MEDWIN PUBLISHERS
Committed to Create Value for Researchers

International Journal of Paleobiology & Paleontology
ISSN: 2642-1283

Ferromanganese Crust: Is a Type of Cenozoic Black Stromatolite in Seabed? The Case of the Rio Grande Rise, South Atlantic Ocean

Cavalcanti JAD*[1] and Santos RV[2]

[1]Geological Survey of Brazil – CPRM, Brazil

[2]Laboratory for Geodynamic, Geochronological and Environmental Studies, Geoscience Institute of Brasília University, Brazil

***Corresponding author:** Jose Adilson Dias Cavalcanti, Geological Survey of Brazil – CPRM. Regional Superintendence of Belo Horizonte, Minas Gerais State, Brazil, Email: jose.adilson@cprm.gov.br

Research Article

Volume 5 Issue 1

Received Date: February 09, 2022

Published Date: March 04, 2022

DOI: 10.23880/ijpbp-16000129

Abstract

Ferromanganese crusts (or Fe-Mn crust) on the Rio Grande Rise (RGR) in the South Atlantic were analyzed on the view point their structures and chemical composition. The main structures of the ferromanganese crusts are wave-layered, columnar, botryoidal and oolite, which are very common in stromatolites. The microstratigraphic succession of the ferromanganese crusts of RGR comprises an older phosphatized crust on the base, and a younger non-phosphatized crust on the top. Mn and Fe are the main compositional elements of the young non-phosphatized crust, with an average concentration (wt%) of 19.04% and 16.07%, respectively. The Fe/Mn ratios average 0.85 indicate the hydrogenous origin of these deposits. In these ferromanganese crusts the average concentrations (wt%) of Co, Ni, Pb, Ti, Cu and Ce are 0.92 %, 0.34 %, 0.25 %, 0.03 %, 0.92 % and 0.15 %, respectively. By comparison, in the old phosphatized crust, the main compositional elements are CaO and P2O5, with an average concentration (wt%) of 34.77% and 15.93%, respectively. In this latter type of crust the ore forming elements content is less and only the Ni concentration is noticeable (0.41%), while the average concentrations (wt%) of Co, Ti, Cu, Pb and Ce are 0.18%, 0.04%, 0.2%, 0.02% and 0.02%, respectively. Graphs of C_{eSN}/C_{eSN^*} ratio vs Y_{SN}/H_{oSN} ratio indicate that old phosphatized crusts is diagenetic and young non phosphatized crust is hydrogenous. In spider diagrams of REY, old phosphatized crust show positive Y anomaly and young non phosphatized crust show positive anomaly of Ce and negative anomaly of Y. Based on available literature, the comparison between the microbial diversity in deep-sea ferromanganese crusts and in stromatolites confirms this similarity. Microbial assemblages in samples from the RGR showed the dominance of the classes gammaproteobacteria, alphaproteobacteria, and deltaproteobacteria, as described for others ferromanganese crusts deposits around the world (Western Pacific Ocean, Clarion-Clipperton zone of the Pacific Ocean, South China Sea, Central Atlantic Ocean and Central Indian Ocean Basin). The results led us to the interpretation that these crusts can be originated from biogenic-hydrogenous processes and they can represent a type of black stromatolites on the seabed, deposited between 17.6 and 14.6 Ma ago.

Keywords: Stromatolites; Fe-Mn Crusts; Rio Grande Rise; South Atlantic Ocean

Abbreviations: RGR: Rio Grande Rise; WR: Walvis Ridge; CFB: Continental Flood Basalts; ERGR: Eastern Rio Grande Rise; WRGR: Western Rio Grande Rise; SEM: Scanning Electron Microscopy; BSE: Backscattering Electron; EDS: Energy Dispersive Spectrometry; TIMS: Thermal Ionization Mass Spectrometry; CFA: Carbonate Fluorapatite; REEs: Rare Earth Elements; BIFs: Banded Iron Formation.

Introduction

The traditional interest in ferromanganese crusts has been in metals such as cobalt, nickel and manganese [1]. Research in the last decades has shown that there is also an economic potential for rare earth elements, titanium, phosphorus, platinum, thallium, tellurium, zirconium, tungsten, bismuth and molybdenum, as well as a potential for studying paleoceanographic and paleoclimatic interactions [1-8]. These crusts occur at depths ranging from 400 to 4000 m, but commonly at depths between 1000 and 3000 m, with precipitating rates of 1-6 mm/Ma which favors their enrichment in most elements of the periodic table [9,10]. They form pavements on consolidated substrates of the ocean floor (plateaus, flanks of the rises, ridges and abyssal regions) by a combination of hydrogenous and biogenic processes [9,11-18].

Wang, et al. [14] reported on the presence of large assemblages of coccoliths/coccolithophores in ferromanganese crust samples of seamounts from the Cape Verde archipelago, and proposed that crust formation is the result also of biomineralization processes. In Clarion-Clipperton Zone, Wang, et al. [19] describe bio-seeds as responsible for deposition of Mn (IV) minerals to form polymetallic nodules. The investigation about microbial diversity in cobalt-rich crusts conducted by Liao, et al. [13] showed that the microorganisms play an important role in the formation of crust as well as in metal recycling. A detailed investigation in samples of the Magellan seamount and Clarion-Clipperton province, carried out by Avdonin, et al. [15], indicates that the primary textural element of oxide ores resulted from the microorganism activity. These authors consider that cobalt-bearing crusts and deep-water nodules are associated with a special type of ferromanganese stromatolites.

In many parts of the world ocean the ferromanganese crusts have a layered structure characterized by the intercalation of ore bearing layers and biogenic and non-biogenic barren materials [20]. The main growth structures described include botryoids, ooids or micro-nodules, columns, laminations and disordered mottled zones [21]. In four seamounts next to Marshall Island were described ferromanganese crusts with layers enrichment in hydrogenetic (Mn, Co, Ni and Mo), biogenic (Cu, Zn and Ba) and detrital (Al, Rb and Ti) elements [22]. Another very common aspect is the presence of phosphatized layers that occur as filling in parallel and vertical cracks. They were interpreted as induced by upwelling of phosphorous-rich deep waters at the slope of seamounts during the expansion of the Antarctic glaciation and intensification of ocean circulation [23], or from suboxid phosphate-rich water of the extended oxygen-minimum-zone infiltrating and preventing precipitation of ferromanganese crusts [24].

The present study proposes that ferromanganese crusts can be a new type of stromatolite that development on the ocean floor, based on the similarities between both, as regards the origin and internal structures. Polymetallic nodules and crusts have recently been recognized as biominerals that are formed around bio-seeds [19], despite of the controversial between biogenic or abiotic origin. One the most important evidence in support biogenic origin is the occurrence of fossilized microbes [25].

The similarity between growth structures of ferromanganese crusts and stromatolites is notable. Jenkyns [26] has first reported this similarity in Jurassic fossils found in nodules of the Alps (Sicily), Carpatho-Balkan chain and others parts of the Mediterranean region. Akai, et al. [27] describe Precambrian Fe-Mn stromatolite or "black stromatolite" in Western Australia, composed of carbonate and todorokite. The main differences is at the origin of these structures, whether they are biogenic or not. Stromatolites are defined as layered sedimentary structures produced by mat-building phototrophic organisms (usually cyanobacterium) and are considered as the most ancient biological record and earliest evidence of the emergence of life on Earth [28]. According to this author, modern stromatolites exist in areas where most other life forms are considered less desirable, such as in extreme environments containing hypersaline water, high alkalinity, and high or low temperatures zones. Different types of stromatolites are described in the literature occur in limestone, phosphates, sulfates and BIF's (Banded Iron Formation). They represent a complex system of nested, physically, chemically, and biologically influenced components that range in scale from microscopic to macroscopic [29]. These components consist of microorganisms, organic compounds of microorganisms, sediment grains, precipitated sediment, sedimentary textures (fabrics), microstructures, laminae, domes, columns, branched columns, and cones.

Stromatolites of aphotic origin and formed in deep water, are less commonly preserved in the sedimentary record than their shallow-water counterparts. They are associated with omission surfaces, hardgrounds, and/or condensed sediments and have been fossilized by authigenic mineralization processes such as the precipitation of iron and manganese oxyhydroxides or phosphates [30]. Lozano & Rossi [31] described stromatolites in El Soplao cave (north Spain) that are formed by polymetallic Mn-rich oxides with subordinate and variable amounts of detrital material. They exhibit dentritic and laminar microfacies, with abundant microbial forms typical of Alpha-Proteobacteria, and probably represent the best example of microbial preservation in ferromanganese deposits described in the literature. In the desert region of Salta in northwestern

Argentina, near the border with Chile, characteristic stromatolite-like ecosystems were discovered lying and developing in shallow hypersaline lakes located above 4,000 m elevation [32]. This environment is characterized by harsh conditions that are very similar to those present in the early Earth atmosphere. These examples of modern and fossilized stromatolite formations appear similar in terms of environment, morphological description, and biological and mineralogical composition.

Geologic Setting

The Rio Grande Rise (RGR) and its eastern counterpart, the Walvis Ridge (WR), represent the two largest bathymetric features away from the South Atlantic Mid-Ocean Ridge (Figure 1a). The origin of the WR has been principally defined as a hotpot trail derived from the Tristan-Gough deep mantle plume and stretching from the Etendeka continental flood basalts (CFB) province in Africa [33-35]. The RGR, located about 1300 km east from the Brazilian coast, between parallels 28°-35° South and meridians 29°-39° West, has on the other hand a more complex geology. Moreover, it has been less sampled by rock dredging and core drilling, making its geological interpretation an ongoing matter of debate. The RGR, with depths as shallow as 800 mbsl and separated from the São Paulo Plateau by the Vema Channel, is composed of two areas with distinct morphologies and geological histories [36] : the Eastern Rio Grande Rise (ERGR) and the Western Rio Grande Rise (WRGR) (Figure 1b). These two morphological features have in common to be intersected by the Cruzeiro do Sul Rift, a NW-SE trending deep sub-marine valley up to 30-40 km wide. The ERGR rises along a north-south trend, parallel to the present Mid-Atlantic Ridge, and is bounded by fracture zones. It has been preliminary interpreted by Gamboa and Rabinowitz [36], as an abandoned spreading center. The WRGR, from which originate all the studied ferromanganese crust samples, forms a widespread bulge that includes seamounts and guyots protruding through or juxtaposing with this platform. Its geological interpretation has been guided until now by spared geological and geophysical information. This is exemplified by the petrographic and geochemical interpretations of the basement rocks that were drawn from only one drilling site (DSDP Site 516F) and very few dredging localities.

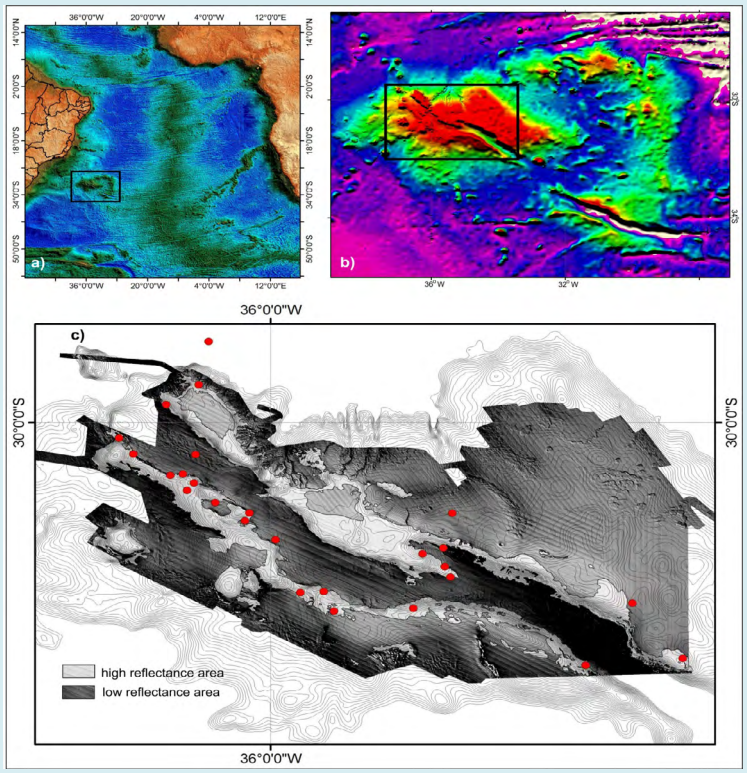

Figure 1: a) Location map of the Rio Grande Rise (RGR) in the South Atlantic Ocean, extracted from the National Oceanic and Atmospheric Administration (http://www.noaa.gov/, access in November 2014); b) detail of the Rio Grande Rise with the location of its western portion (WRGR) studied; c) detail of the WRGR with bathymetry and backscattering fusion map showing high reflectance areas of prospecting cobalt-rich crusts and locations of the dredged samples used in this study (depth range between 2500 and 695 m) – see Table 1

Volcanism

The basement at this drilling site consists of tholeiitic basalt which was Ar-Ar dated by Rohde, et al. [37] at 80-87 Ma - Santonian (Late Cretaceous) - in good agreement with the predicted age of the oceanic crust for this region based on the magnetic anomaly data. This also suggests that the WRGR formed at or close to a spreading center [35,36,38]. It is worth noting that this age coincides with the intrusion ages of most of the onshore alkaline intrusions in Brazil (e.g. the Poços de Caldas region) [39]. In contrast, rocks dredged from the guyots protruding from this platform have alkali-basaltic composition as characteristic for intra-plate ocean island basalts [40], with one of these samples that was Ar-Ar dated by Rohde, et al. [37] at only 46 Ma (Mid Eocene). The occurrence of ash layers and volcanic breccia in cored sediments of the same age at DSDP Sites 516 and 357 is another indication that a widespread volcanic-tectonic event affected the WRGR region during the Mid Eocene. It is believed that the RGR has been uplifted by up to 700 m during this event which coincides with the formation of the transtensional Taubaté Basin onshore and the formation of alkaline volcanic rocks in the area of Rio de Janeiro and within the Eocene sequence of the Santos and Campos Basins [39]. During this event parts of the WRGR plateau were uplifted above sea level and several short-lived volcanic islands were created, which were later submerged as the plateau subsided [36,38]). The associated paleoenvironmental changes, i.e. ocean circulation pattern and water column characteristics (depth, temperature, dissolved oxygen concentration, luminosity, salinity), may have played an important role in the development of favorable conditions for the formation of stromatolites and the deposition of Co-rich ferromanganese crusts.

While the current geological understanding for the origin of the RGR, as mentioned above, mainly argues in favor of a thick oceanic crust made mostly of basalts, recent geophysical studies indicate that it may also be partially made of continental crust [38,41]. This hypothesis has been strengthened by the recovery at the WRGR of continental crustal rocks (granite, gneiss, granulite) of Precambrian age and the direct observation from the Japanese submersible Shinkai 6500 of a porphyritic granite rock pavement with more than 5 m in extension [42]. These important new findings imply to revise the interpretation on the origin of the Rio Grande Rise and on the South Atlantic tectonic evolution as a whole. During continental rifting, fragments of material from the continental margins may be detached and surrounded by oceanic crust, as microcontinents in the ocean basins. Seismic studies and drilling results have shown that the Kerguelen Plateau in the Indian Ocean is underlain at least in part by continental crust [43-45]. Since the RGR (Atlantic Ocean), Kerguelen (Indian Ocean) as well as the Jan Mayen (Arctic Ocean) microcontinents are associated with hotspots, this suggests that deep mantle plumes may play a role in their formation by weakening the local lithosphere prior to breakup. Alternatively, detachment of continental material during breakup may control the location and composition of subsequent intraplate volcanism [46]. A new petrographic and geochemical study is being carried out on a more complete set of dredged volcanic rocks which should help in refining the interpretation of the RGR formation (Christian Lacasse pers. comm., January 2015).

Sedimentation

Sediments on the RGR have been described in details from the cored sections of DSDP Hole 516F, located on the northeastern flank of the RGR. The sequence begins with basal sediments of about 82 Ma old (Late Cretaceous). The stratigraphic succession mainly comprises limestones that are divided into eight lithostratigraphic units that are distinguished by their lithification and diagenesis degree. The first seven units are represented by a continuous succession of pelagic carbonates interbedded with volcanogenic sediments while the lowermost unit (Unit 8) is in contact with basalts of the bedrock [47]. According to these authors, the carbonate rocks sequence is almost continuous from Santonian-Coniacian to Recent, with only one observed discontinuity in the Upper Miocene. Several important geological boundaries were identified such as the Cretaceous/Tertiary, Eocene/Oligocene, and glacials/interglacials of the Lower Pliocene.

The stratigraphic succession can be summarized upward as follows: i) basal unit (Unit 7) between 1270-1240 m below seafloor (mbsf), composed of ferruginous cherts, limestones, glauconite-rich sandstones, turbidites, and shallow water microfossil (1252-1240 mbsf); ii) Unit 6, between 1240-1000 mbsf, composed of malm limestones intercalated with micritic limestones containing nannofossils, microcrystalline limestones and shales; iii) Unit 5, between 1000-874 mbsf, formed by limestone and calcareous malm, gray in color, with some thin layers alternatively enriched in organic matter or carbonate; iv) Unit 4, between 874-634 mbsf, mainly consisting of foraminiferous and calcareous nannofossils, interlayered with greenish gray montmorilonitic volcanic ash; v) Unit 3, between 634-332 mbsf, formed by chalk, composed of nannofossils occasionally mixed with foraminifers; vi) Unit 2, between 332-193 mbsf, composed of mud with nannofossils and foraminifers, with parallel laminations; vii) and Unit 1, between 193-0 and mbsf, composed of calcareous mud flats with nannofossils and foraminifers.

Materials and Methods

Sample Collection

Before collecting the crust samples on the Rio Grande Rise, multi-beam surveys of high definition (bathymetry, sub-bottom and back scattering) were performed and completed by micro seismic profiles. The samples were collected during R/V Marion Dufresne cruises Leg 1 and Leg 2, using rectangular and circular dredges with the assistance of a TV Grab system which allowed additional sampling and filming of the seabed.

The locations of the dredged samples are shown in figure 1c and the dredging coordinates and sample description are summarized in Table 1.

No	Station	Depth, m	Start Lat.	Start Long.	Final Lat.	Final Long.
1	DC-005	1345 - 1225	-30.558989	-36.116371	-30.33541	-36.073223
2	DC-010	1740 - 1640	-30.955885	-35.020271	-30.946175	-35.038647
3	DC-011	1833 - 1582	-30.559913	-35.010909	-30.573793	-35.000617
4	DC-012	1131 - 1060	-30.72558	-35.974075	-30.755189	-34.98418
5	DC-015	1022 - 1013	-31.117647	-34.030161	-31.117697	-34.040247
6	DC-017	1218 - 1150	-31.458661	-33.755455	-31.468037	-33.76457
7	DC-018	912 - 705	-29.49891	-36.337953	-29.84485	-36.548061
8	DC-021	1772 - 1462	-30.197883	-36.410906	-30.189643	-36.410352
9	DC-025	1088 - 702	-30.419412	-36.456264	-30.700154	-36.016902
10	ML-001	1689 - 1439	-29.89	-36.57	-29.8403	-36.58
11	ML-003	801 - 695	-29.766581	-36.392223	-29.792929	-36.394062
12	ML-011	990 - 950	-30.495476	-36.302307	-30.486013	-36.302361
13	ML-014	1500 - 1354	-30.6073	-36.1403	-30.583598	-36.140062
14	ML-015	930 - 946	-31.1667	-35.6565	-31.166643	-35.643917
15	ML-024	1600 - 1460	-30.7765	-35.0599	-30.75335	-35.060083
16	ML-039	830 - 800	-31.148266	-35.223911	-31.15989	-35.214233
17	ML-041	1330 - 1240	-31.051773	-35.83852	-31.052992	-35.81918
18	ML-049	1580 - 1205	-31.500224	-34.284083	-31.5111	-34.2838
19	ML-064	1105 - 995	-30.81112	-35.172832	-30.8207	-35.1787
20	ML-065	1600 - 1500	-30.89218	-35.05249	-30.904486	-35.058868
21	ML-067	1000 - 950	-31.045689	-35.711288	-31.0483	-35.7109
22	ML-068	895 - 855	-31.1667	-35.6565	-31.166643	-35.643917
23	ML-073	1350 - 1290	-30.195063	-36.749195	-30.208832	-36.748817
24	ML-075	1440 - 1376	-30.318943	-36.479797	-30.332474	-36.485876
25	ML-076	1420 - 1304	-30.326317	-36.548233	-30.3398	-36.548323
26	ML-077	1542 - 1200	-30.0967	-36.8273	-30.1049	-36.8276
27	ML-078	1300 - 1200	-30.3748	-36.4195	-30.4148	-36.4356

Table 1: Dredging locations of ferromanganese crusts on the Rio Grande Rise.

Optical and Electronic Petrography

The textures and structures were characterized in thin sections by optical microscopy using transmitted and reflected light and scanning electron microscopy. Hand specimens were previously classified in two morphological groups based on macroscopic observations, between plate-like (flat and concretion) and nodule-like types.

The analysis by scanning electron microscopy (SEM) was done on a Zeiss LS15 microscope in the mineral analysis laboratory (LAMIN-BE) of the Belém Regional Superintendence of the Geological Survey of Brazil. The polished slides were covered in high vacuum with a 20 m

thick carbon film. The emission filament is tungsten and the high vacuum mode (3.0 - 1.5 x 10^{-5} mPa) was used for electronic imaging and chemical analysis. Backscattering electron (BSE) images of minerals and textures were obtained at a voltage of 20 kV, inrush current of 60 to 90 pA, working distance of 8.5 mm, and magnification between 60 and 2000 times. The chemical composition of the minerals was analyzed by energy dispersive spectrometry (EDS) on an Oxford Instruments X-Act SSD 10mm^2 detector. Analytical results were also acquired at a working distance of 8.5mm and with a voltage of 20kV, but with an incoming current between 170 and 200 pA to maintain an output count rate of about 2000 cps

Litogeochemical Analysis

The chemical analyses were performed at Acme Analytical Ltda., in Vancouver, Canada. Concentrations of traces elements and rare earth elements were determined by ICP-MS, after fusion with lithium metaborate and digestion with nitric acid. The major oxides and some metals elements were determined by X-ray diffractometry (PANalitical Axios) after fusion with lithium metaborate, lithium tetraborate and sodium nitrate. Later, using optical microscope and geochemistry analyzes, the samples were classified between Fe-Mn-rich and Ca-P-rich crusts.

$^{87}Sr/^{86}Sr$ Ratio Measurement

$^{87}Sr/^{86}Sr$ ratios of the substrate on ferromanganese sample HS-145a and on a carbonate vein in sample ML11D were determined through TIMS (Thermal Ionization Mass Spectrometry), in a Finningan MAT 262 at the University of Brasília. Samples were digested in H_3PO_4 and the residue kept in a HNO_3 (2.9 N) solution for column chromatography. The solution containing Sr was collected, dried and then dissolved in 1 ml HNO3 (50%) for analysis. Procedures followed steps used by Alvarenga, et al. (2007). NBS-987 was used as reference material, and yielded a $^{87}Sr/^{86}Sr$ ratio of 0.71028 ± 1 (1σ).

Ferromanganese Crusts of Rio Grande Rise

The ferromanganese crusts (or crusts herein) of the Rio Grande Rise are located on the top and slopes of elevated topographic areas. To define the types of ferromanganese crusts, images of seabed generated from the TV Grab and macroscopic description of samples collected during expeditions were used (Figure 2). The crusts occurring on top, mainly on calcareous rocks, form pavements or layers (plate-like) with a thickness ranging from 2 to 15 cm, and also concretions (nodule-like) with diameters between 5 and 15 cm at depths between 900 and 1500 m. The crusts occurring on the slopes form irregular masses overlying fragments of volcanic rocks and, more rarely, limestone and calcareous phosphate rocks (film-like) in depth between 1200 to 2800 m. Macroscopically, the ferromanganese crusts can be subdivided in different groups, based on their morphology, structure and texture, between laminated, layered, botryoidal, coralloid, concretions and massive crusts.

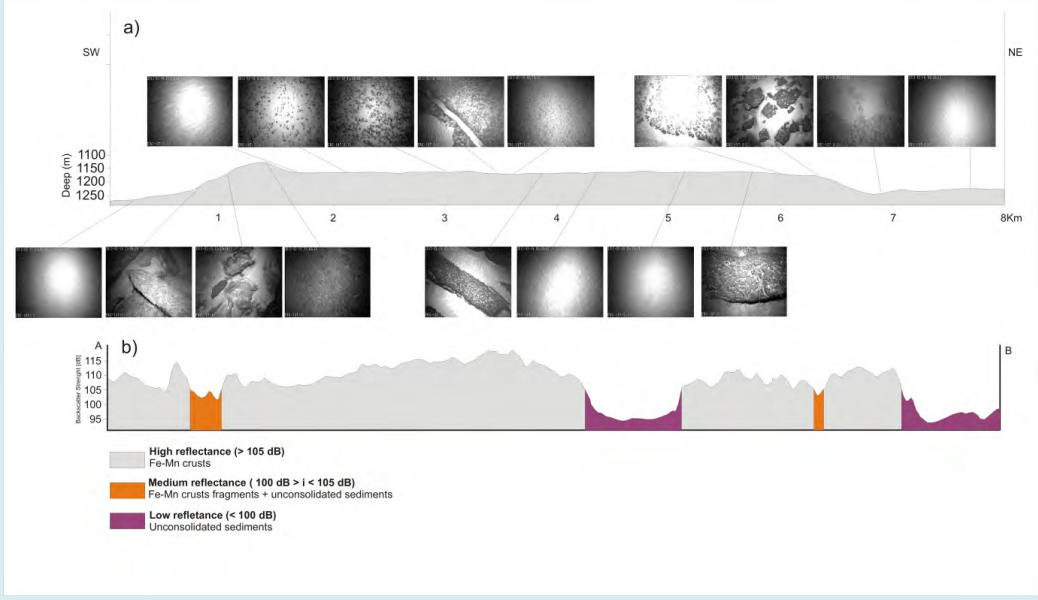

Figure 2: Bathymetric (a) and reflectance (b) profile of the marine substrate. Images acquired using the TV Grab system and showing the main types of ferromanganese crusts on the Rio Grande Rise.

In the top they occur in the form of pavement or layer (plate-like) with thickness that varies from 2 to 10 cm, and also in the form of concretions (nodule-like) with diameters between 5 and 15 cm, in depths between 900 and 1500 m. On the slopes they constitute an irregular mass that occur covering fragments of volcanic rocks and, more rarely, calcareous and calcareous phosphate (film-like) rocks.

In terms of stratigraphic succession one has an older phosphate crust at the base, separated by a discontinuity (depositional hiatus) from the younger non-phosphate crust (Figure 3). In the non-phosphate crust at least three millimeter layers of phosphate carbonate rock were identified that may represent depositional hiatuses that occurred in the South Atlantic.

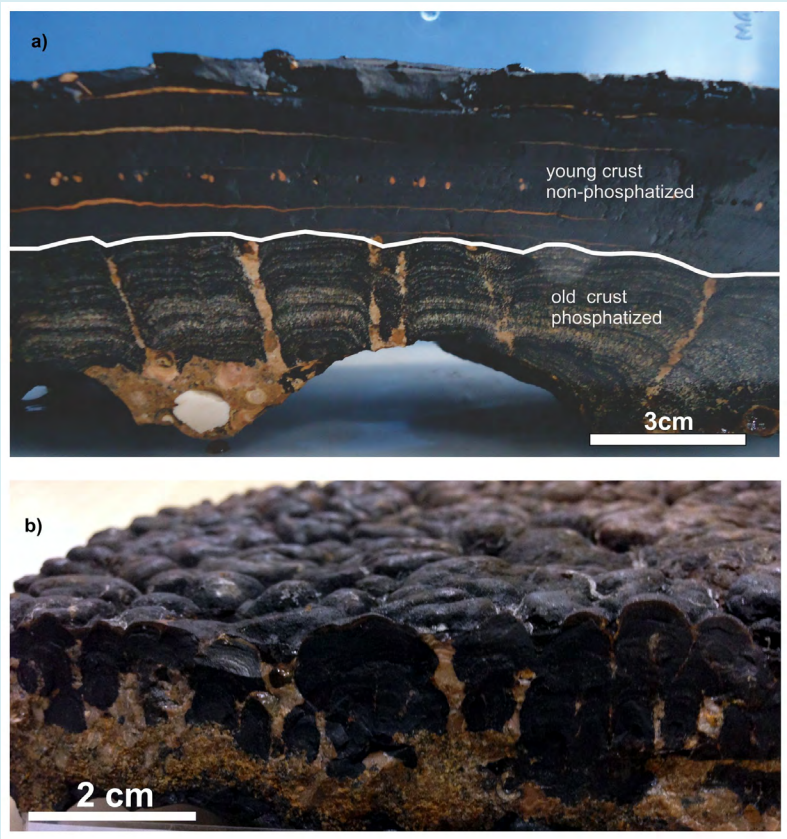

Figure 3: Photographs showing (a) the stratigraphic sequence and (b) stromatolite-like structures of ferromanganese crusts of the Rio Grande Rise.

Petrography

The petrographic characterization of the ferromanganese crusts was performed on the basis of both their morphological (plate-like vs. nodule-like) and geochemical (Co-rich vs. P-rich) classifications. The micro stratigraphic sequences consist of the P-rich crusts at the base and Co-rich crusts at the top (Figure 3). Internal structures can be grouped either as sedimentation structures or as discontinuities. Sedimentary structures can be wavy-layered (or plane-parallel stratification), parallel columns, branching columns, botryoidal and nodular. The transition from one structure to another may be gradual or abrupt. When abrupt, the transition can represent change in the characteristics of the sedimentary environment (changed facies) but also a depositional hiatus.

Wavy-layered Structure*:** Is very similar to algal mats of common stromatolites. Its typically exhibits undulations and is defined by the intercalation of light and dark layers generating a micro-banding (Figure 4a). They are more common on the basis of Co-rich crusts, and also on the basis of various depositional cycles, marking the change of a depositional cycle. It often contains materials that may represent micro detrital carbonate. In the Co-rich crusts the clear layers predominate whereas in the P-rich crusts the proportion of darker layers increases. Gradual facies variations were observed between P-rich and Co-rich crusts. ***Columnar Structure: Is also very similar to that occurring in common stromatolites. It exhibits simple columns (parallel) or has a branching (composite) or more complex (random) aspect (Figure 4b and 4c). Usually they occur in the middle layer of the crusts, having wavy-layered structure at the base,

characterizing the beginning of a new depositional cycle. Despite this columnar aspect a plan-parallel layering can be observed on a larger scale. The micro-banding, defined by the intercalation of light and dark layers, is similar to bacterial mats observed in common stromatolites.

Botryoidal Structure: It mainly occurs in P-rich crusts and is formed by the intercalation of light and dark layers, the latter being more predominant. This type of structure is very similar to the common botryoidal morphology observed on the surface of ferromanganese crusts. It can also appear scattered between the layers of P-rich crusts (Figure 4d). The limestones layers are formed by deposition of fossiliferous sediments.

Micro-nodule Structure: This structure is more common on top of the ferromanganese crusts. It is generally observed with a gradational change from random structures to nodules. Initially the shapes are very irregular and gradually change to a more regular aspect (Figure 4e). This type of structure occurs in Co-rich crusts and is formed by intercalation of light and dark concentric thin layers that materialize the shape of the oolites. Apparently these structures do not have a germination nucleus.

Discontinuities: These structures are apart from those described before and mark changes in depositional environment and/or interruption of sedimentation cycle (Figure 4f). They can be either plane-parallel (concordant) in aspect, reflecting changes in the depositional environment, corresponding to erosional surfaces (discordant), marking the beginning of a new cycle or depositional hiatus, or representing a lateral change of facies.

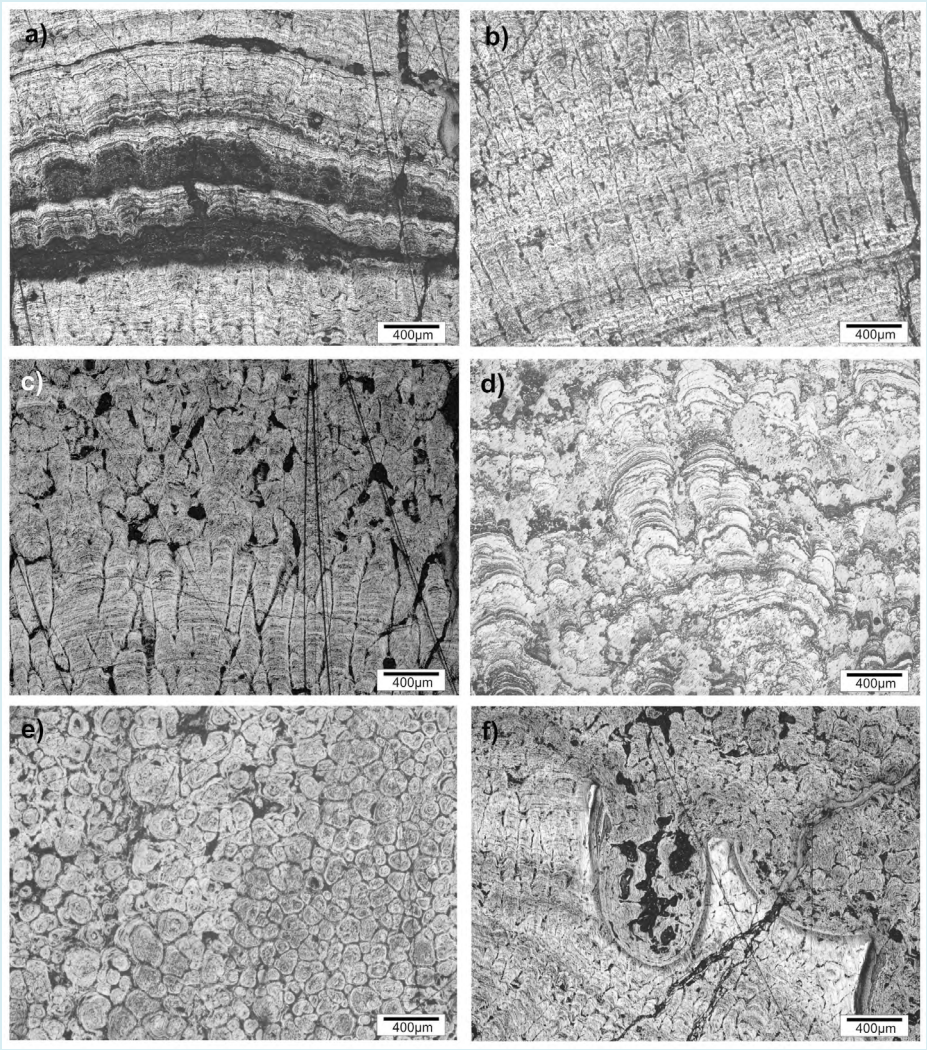

Figure 4: Photomicrographs of the optical microscopy showing the main sedimentary structures of ferromanganese crusts. a) wavy-layered structures marked by undulation nd intercalation of dark and light layers; b) parallel columns; c) branching columns and random structures; d) botryoidal structures with biofilms; e) micro-nodules or oolites structures; f) unconformity between two depositional cycles.

Stratigraphy

Their stratigraphic succession comprises an older phosphatized crust (P-rich crust) at the base and a younger non-phosphatized crust (Co-rich crust) at the top, both being separated by a discontinuity (depositional hiatus) (Figure 3a). In the younger non-phosphatized crust, at least three layers of phosphate-carbonate rock, several millimeters thick, were identified. They may represent depositional hiatuses that have occurred in the South Atlantic Ocean.

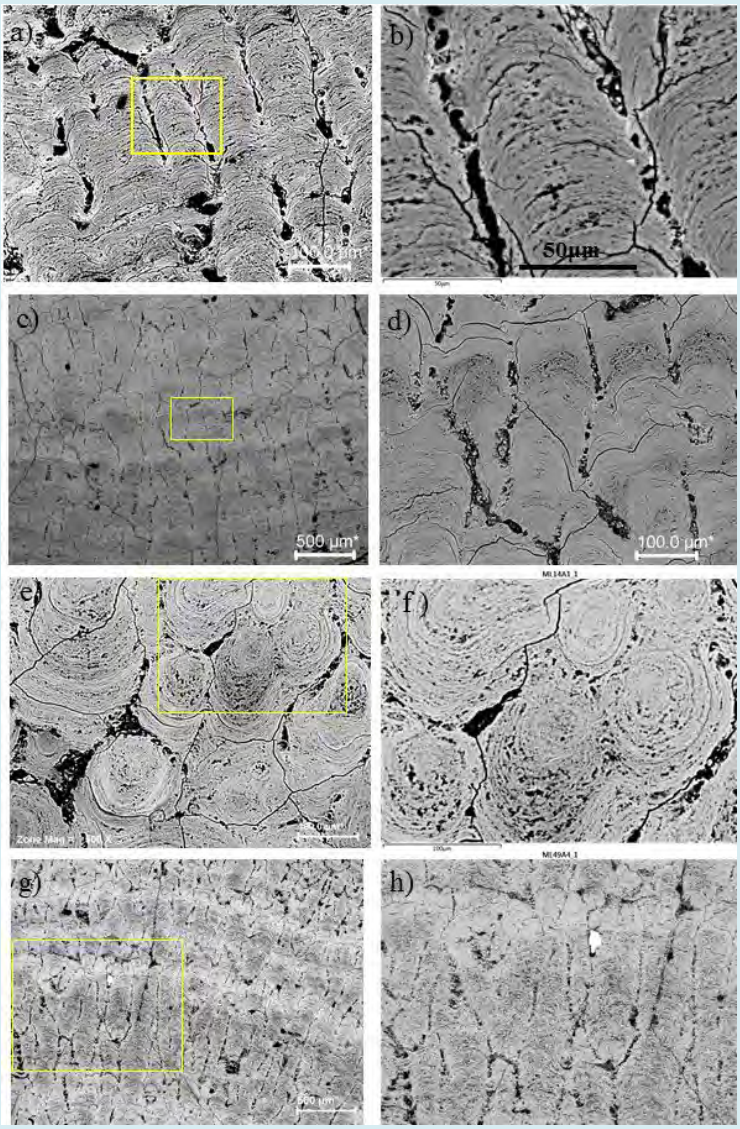

Figure 5: Main sedimentary structures observed on scanning electron microscopy. a) and b) Columnar structures in the plate-like planar Fe-Mn crust, composed mainly of Fe-vernadite, and containing hydrogoethite at the edges of the columnar structure and vugs containing fragments of ferruginous material and detrital silicates; c) and d) detail of the columnar structure showing the space between the columns filled by fragments and detrital crust and silicates, composed of Fe-vernadite, amorphous Fe-Mn oxyhydroxide at the edges and vugs containing fragments of ferruginous material and detrital silicates; e) and f) details of the micro nodular structures in the nodule-like cobaltiferous crust. The vug is filled with fragments of the Fe-rich crust, and carbonate; g) and h) columnar structures on top of film-like crusts containing detrital material in the boundary zone of the columnar structures.

The old phosphatized crusts correspond to the basal section of ferromanganese crusts of the Rio Grande Rise. They have a maximum thickness of 10 cm, a smooth botryoidal irregular surface, banded internal structure with

up to seven layers that can be visually distinguished (Figure 6.). A series of parallel fractures, filled with carbonate-phosphatic material, intersect the crusts. Observation through the microscope shows slight banding defined by the alternation of ferromanganese layers and carbonate-phosphate bioclastic layers. These layers enriched in bioclastic carbonate-phosphatic material are repeated throughout the crust. The main structures of P-rich crusts are botryoidal and wavy-layered. Some structures are delineated by thin layers of a very dark material that can be organic matter. In a complete thin section, seven layers which were subdivided into twenty-three facies characterized by alternation of depositional cycles that begin with bioclastic carbonate deposition and carbonaceous material, followed by the deposition of ferromanganese crust (Figure 6). The carbonate portions are composed mainly by foraminifers.

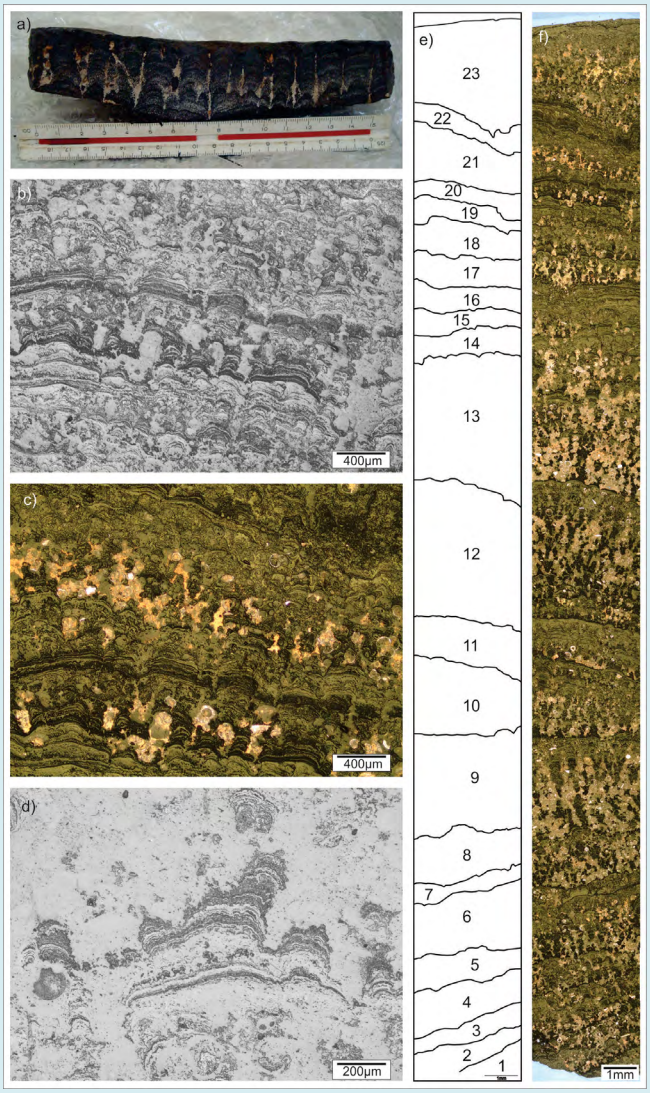

Figure 6: Images of an old phosphatized crust. a) hand specimen (scale of 15 cm) showing banding structures of P-rich crust; b) and c) black biogenic structures in reflected and transmitted light under the microscope; d) detail of black biogenic structures in reflected light under the microscope; e) and f) profiles of crust with interpretation of depositional cycles.

The young non-phosphatized crusts can be plate-like flat, plate-like concretion and Nodule-like. Plate-like flat show botryoidal surficial morphology, inner columns and wavy-layered structures with at least five distinctive depositional layers, more or less well defined, with a total thickness ranging between 55 and 90 mm (Figure 3). Micro nodular structures predominate at the base of these crusts and are progressively replaced upward by columnar structures. The columnar structures have a parallel lamination with attenuated color variations that may reflect the involvement of biogenic components. The portions of crusts, appearing clearer under the reflected light of the microscope, indicate

an environment with the precipitation of manganese oxides whereas the darker portions of the crusts may represent algal mats with relics of bacterial films deposited between manganese oxide layers. Another obvious structure is an erosive discordance that may reflect a depositional hiatus between two different crusts.

Plate-like concretion exhibit a smooth botryoidal morphology at their surface including five distinct wavy layers (Figures 7a and 7b). Their total thickness is about 140 mm. The core consists of several fragments of carbonate-phosphate-rich rocks. Analysis of a complete polished thin section indicates nine individual depositional cycles with predominance of columnar, and more rarely wavy- layered, brotryoidal, oolite or micro-nodule structures (Figures 7c and 7d).

Nodule-like are concretions of various forms, from flattened oval to even irregular, with variable diameters, containing the carbonate-phosphate core (Figure. 7f and 7g). They occur at depths between 900 and 1500 m and have diameters between 5 and 20 cm. Under the microscope, the crust displays columnar, wavy-layered, botryoidal and micro-nodular structures. In this type columnar structures predominate and can be parallel and branching. The transition from one structure to another can be abrupt or transitional. When abrupt, we considered that can be a depositional hiatus. Near to the core of the nodule, the layers are very irregular and, toward the top, the structures become more regular. In micro-stratigraphic profile was possible to distinguish different layers and also different facies, which may reflect changes in the characteristics of the depositional environment of the ferromanganese crust.

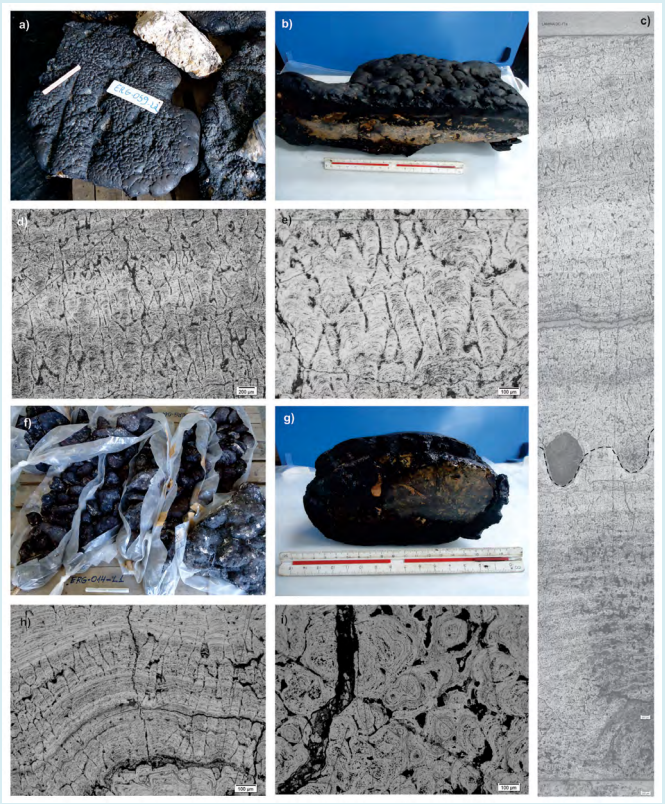

Figure 7: Images of an young non-phosphatized crust: a) and b) hand specimens of plate-like crust (scale of 15 cm) with botryoidal surficial habit and plate-like crust section, respectively; c) thin section profile in reflected light under the microscope of plate-like crust with hiatus surface; d) and e) columnar structure and detail of columnar structure, respectively, in reflected light under the microscope; f) and g) hand specimens of (scale of 15 cm) nodule-like crust and section; h) and i) wavy-layered and columnar structures of nodule-like crust and micro-nodule structure of crust, respectively, in reflected light under the microscope.

Mineralogy

XRD data obtained by Souza, et al. [48] in Fe-Mn crusts of Rio Grande Rise revealed that non-phosphatized layers of the samples are mainly composed of Fe-vernadite (δ-MnO_2), and calcite and quartz may be present to a lesser extent. Older phosphatized samples are composed of a stable 10 Å Mn-phase (todorokite) instead of a Fe-vernadite. Carbonate

fluorapatite (CFA) and calcite are present in all phosphatized samples.

Geochemistry

Chemical analyses of major, minor and rare earth elements (REEs) were carried out on 49 crust samples, including 42 of Co-rich and 7 of "P-rich" type (Table 2). The predominant components of young non-phosphatized crust are Mn and Fe, and in old phosphatized crust are $CaCO_3$ and P_2O_5. The ore forming elements are Co, Ni, Pb, Ti, Cu and Ce.

PLATE-LIKE PLANAR							
Sample	1	2	3	4	5	6	7
SiO_2	1,43	1,27	1,43	1,77	1,35	1,22	1,59
Al_2O_3	2,56	1,14	1,68	2,14	1,20	2,25	2,00
Fe_2O_3	6,75	9,38	7,31	6,66	6,78	4,52	3,15
MnO	9,90	12,82	12,11	7,02	13,21	11,44	12,00
CaO	34,01	30,42	32,67	38,01	32,49	37,69	38,12
MgO	3,59	2,25	2,74	2,54	2,14	3,32	3,13
Na_2O	1,02	1,32	1,16	0,96	1,36	1,01	1,09
K_2O	0,22	0,27	0,28	0,24	0,34	0,20	0,30
TiO_2	0,35	0,59	0,48	0,20	0,43	0,23	0,22
P_2O_5	16,76	13,33	16,66	16,30	16,12	15,78	16,54
LOI	22,0	25,5	21,8	23,1	23,0	20,8	20,3
SUM	97,16	97,02	96,89	97,17	97,07	97,24	96,85
Co	1273,5	3278,7	1934,6	983,2	2330,1	1866,5	1221,0
Ni	4318	3032	4198	3358	3582	5042	5455
Cu	295,1	108,9	118,3	336,9	107,0	389,0	277,3
Pb	295,5	947,7	586,9	178,1	606,4	309,4	190,8
Sr	1849,3	2106,4	2157,5	1475,0	2196,6	1609,5	1854,9
Zn	388	481	632	327	676	452	535
Zr	135,0	151,2	148,6	86,6	132,3	102,2	97,9
Ba	401	745	932	242	997	458	601
V	425	481	406	312	343	345	252
Mo	166,4	231,5	171,5	155,9	197,1	256,6	155,8
La	130,3	187,9	210,0	71,9	182,0	131,4	124,5
Ce	198,9	611,9	389,2	95,9	359,1	181,3	133,8
Pr	23,01	32,93	36,09	11,97	29,58	20,39	20,05
Nd	102,5	138,7	162,8	55,1	127,8	93,3	91,2
Sm	19,71	27,19	30,29	10,34	23,42	16,55	17,39
Eu	4,92	6,24	7,65	2,48	5,77	3,89	4,13
Gd	25,84	30,85	40,30	12,88	29,87	21,46	22,55
Dy	25,44	26,86	37,30	11,34	26,57	19,88	21,00
Ho	5,89	5,72	8,96	3,06	6,66	4,65	5,42
Er	16,99	17,38	26,81	8,83	19,76	13,45	15,42
Tm	2,27	2,39	3,54	1,20	2,75	1,88	2,10
Yb	13,41	14,09	20,64	7,46	16,98	10,58	11,45
Lu	2,12	2,18	3,35	1,18	2,52	1,78	2,05
Y	240,9	188,9	364,3	131,1	299,5	202,2	234,7
Sc	7	5	8	5	7	6	7
SUM	819,2	1298,2	1349,2	429,7	1139,3	728,7	712,8

a) *Old phosphatized crusts*

(1) **PLATE-LIKE CONCRETION**											
Sample	1	2	3	4	5	6	7	8	9	10	11
SiO_2	2,20	2,52	4,39	2,53	2,35	1,96	2,45	1,92	1,78	2,53	3,46
Al_2O_3	0,73	0,86	1,70	1,09	0,80	0,74	1,39	0,71	0,82	1,07	1,24
Fe_2O_3	21,86	24,20	24,75	24,33	24,88	21,52	21,49	22,07	20,72	22,22	23,77
MnO	23,78	25,18	22,55	24,69	24,18	23,65	23,31	27,41	28,04	26,41	22,37
CaO	3,57	3,34	3,06	3,34	3,83	3,28	7,37	3,71	3,69	3,34	3,80
MgO	1,76	1,92	1,83	1,84	1,83	1,69	2,15	1,94	1,96	1,94	1,88
Na_2O	1,63	1,68	1,65	1,70	1,73	1,72	1,70	1,93	1,91	1,79	1,69
K_2O	0,37	0,41	0,46	0,39	0,40	0,36	0,41	0,41	0,41	0,41	0,39
TiO_2	1,59	1,51	1,71	1,62	1,52	1,64	1,53	1,47	1,56	1,33	1,41
P_2O_5	1,01	1,11	1,02	1,18	1,40	1,07	2,48	1,10	1,10	1,09	1,35
LOI	38,8	34,5	34,2	34,5	34,2	39,4	33,1	34,4	35,1	35,2	36,2
SUM	97,30	97,23	97,32	97,21	97,12	97,03	97,38	97,07	97,09	97,33	97,56
Co	11160	9870	7340	7880	8340	11450	9200	11470	12890	8210	8790
Ni	2822	3169	3186	3746	3548	2996	3580	3513	3550	3838	2756
Cu	267	351	442	345	195	283	466	258	290	374	287
Pb	2460	2635	2139	2719	2792	2583	2634	2864	2809	2705	2526
Sr	1747	1799	1738	1915	1904	1803	1538	1705	1632	1706	1573
Zn	590	650	680	590	610	580	690	610	610	720	650
Zr	373	384	512	400	342	366	330	322	311	333	373
Ba	1271	1367	1657	1475	1491	1299	1453	1158	1121	1433	1048
V	875	988	919	1047	1082	961	807	895	790	963	830
Mo	478	512	465	536	581	466	428	568	521	663	462
Tl	162	179	231	249	242	159	177	203	192	224	124
As	211,2	229,7	182,0	153,3	81,1	241,8	175,2	197,4	211,5	184,0	115,0
La	263	323	281	279	313	265	240	291	249	245	287
Ce	1518	1672	1751	1556	1637	1388	1504	1341	1261	1487	1253
Pr	50	64	55	52	61	51	44	55	45	47	54
Nd	208	261	218	222	248	209	181	224	182	182	223
Sm	40	50	43	43	49	41	34	44	37	38	43
Eu	9	12	10	10	11	9	8	10	9	8	10
Gd	47	57	49	49	53	48	40	49	42	42	50
Tb	6	8	7	7	8	7	5	7	6	6	8
Dy	37	48	42	42	45	39	33	41	35	35	44
Ho	8	10	8	9	9	8	7	9	8	8	10
Er	24	28	24	27	28	26	20	25	23	21	27
Tm	3	4	4	4	4	4	3	4	3	3	4
Yb	20	24	22	24	25	23	17	21	20	19	23
Lu	3	4	3	4	4	3	3	3	3	3	4
Y	144	184	154	185	194	167	152	170	154	127	187
Sc	4	6	7	4	5	4	5	5	5	4	7
SUM	2384	2753	2679	2515	2693	2292	2296	2297	2081	2275	2235

(2) PLATE-LIKE PLANAR										
Sample	1	2	3	4	5	6	7	8	9	10
SiO_2	4,55	1,10	2,90	1,66	3,21	0,91	4,18	4,65	7,34	3,40
Al_2O_3	1,42	0,77	0,98	0,60	1,61	0,57	1,40	1,57	2,86	1,13
Fe_2O_3	23,76	21,26	24,77	22,70	23,28	21,35	25,39	24,15	22,87	26,21
MnO	22,74	23,54	24,02	25,56	24,07	24,11	23,41	21,75	21,73	23,83
CaO	3,05	6,33	3,33	5,51	3,19	7,00	3,21	3,08	3,64	3,27
MgO	1,71	2,40	1,76	1,98	2,04	2,43	1,74	1,63	2,04	1,71
Na_2O	1,80	1,50	1,76	1,68	1,69	1,70	1,69	1,56	1,91	1,65
K_2O	0,43	0,33	0,39	0,38	0,43	0,33	0,43	0,43	0,53	0,42
TiO_2	1,80	1,56	1,46	1,48	1,68	1,47	1,79	1,58	1,77	1,59
P_2O_5	1,07	1,12	1,18	1,11	1,20	1,07	1,10	1,01	1,38	1,11
LOI	34,8	37,2	34,8	34,4	34,7	36,2	33,0	36,1	31,3	33,1
SUM	97,13	97,11	97,35	97,06	97,10	97,14	97,34	97,51	97,37	97,42
Co	10160	8510	8280	9340	9300	8490	7620	7720	6490	6930
Ni	2845	3962	3015	3667	3782	4371	3099	2769	4077	2945
Cu	254	225	184	197	568	235	291	342	742	216
Pb	2570	2426	2461	2528	2522	2557	2363	2224	2207	2433
Sr	1727	1928	1851	2142	1677	1937	1770	1624	1570	1919
Zn	560	540	600	500	720	480	660	650	650	630
Zr	443	323	383	315	420	306	476	437	543	423
Ba	1447	1469	1338	1366	1504	1422	1543	1463	1448	1603
V	894	1012	992	1020	947	1015	954	920	855	1025
Mo	451	425	557	552	470	482	499	471	381	554
Tl	198	136	200	234	250	108	213	192	217	217
As	192,8	270,5	114,8	158,7	174,4	288,2	189,0	177,9	64,2	122,5
La	277	266	311	312	222	275	288	276	206	302
Ce	1876	1428	1422	1460	1444	1412	1838	1728	1520	1867
Pr	53	55	60	62	41	56	55	54	40	59
Nd	217	239	246	253	177	231	229	222	167	239
Sm	42	45	49	49	33	46	45	43	33	47
Eu	10	10	12	12	8	11	10	10	8	11
Gd	49	49	56	54	40	51	51	47	39	54
Tb	7	7	8	8	6	8	8	7	6	8
Dy	41	42	49	46	34	40	42	39	33	42
Ho	8	9	10	9	7	9	9	8	7	9
Er	24	25	29	27	24	25	26	24	21	27
Tm	4	4	4	4	3	4	4	3	3	4
Yb	22	22	26	24	21	22	24	21	20	23
Lu	3	3	4	4	3	3	4	3	3	4
Y	155	175	187	185	154	183	169	140	135	160
Sc	6	3	6	4	5	3	6	6	6	5
SUM	2795	2382	2478	2513	2222	2380	2807	2634	2245	2857

(2) PLATE-LIKE PLANAR											
Sample	11	DC-38a	ML-39a	DC-39a	DC-58a	DC-59a	ML-64a	ML-73c	ML-75a	ML-76a	DC-76a
SiO_2	1,50	4,05	1,24	2,44	6,67	3,29	4,93	5,57	3,72	2,99	3,79
Al_2O_3	0,62	1,89	0,81	0,87	2,38	1,07	2,01	2,16	1,40	1,02	1,38
Fe_2O_3	22,65	25,53	22,84	22,62	25,25	23,34	23,07	24,44	22,53	25,47	24,63
MnO	27,26	23,20	26,73	26,52	22,40	24,24	22,85	23,51	24,91	23,98	23,98
CaO	4,01	3,37	4,89	4,29	2,99	3,28	3,11	3,05	3,53	3,17	3,21
MgO	1,99	1,87	2,26	1,87	1,84	1,68	1,88	1,96	1,97	1,82	1,81
Na_2O	1,85	1,74	1,63	1,83	1,73	1,56	1,73	1,70	2,06	1,66	1,71
K_2O	0,38	0,43	0,34	0,38	0,43	0,37	0,46	0,45	0,46	0,42	0,40
TiO_2	1,52	1,47	1,54	1,49	1,51	1,39	1,65	1,59	1,63	1,59	1,52
P_2O_5	1,12	0,96	1,06	1,43	0,96	1,01	1,07	1,10	1,30	1,07	0,99
LOI	34,2	33,1	34,0	33,6	31,5	36,4	34,8	31,9	33,9	34,3	34,1
SUM	97,10	97,61	97,34	97,34	97,66	97,63	97,56	97,43	97,41	97,49	97,52
Co	11250	7810	7700	9480	6170	7510	7500	6980	8820	7050	7440
Ni	3459	2421	4281	3322	2676	2628	3079	3129	3189	2542	2538
Cu	253	329	223	235	396	239	554	499	422	248	273
Pb	2986	1851	3086	2998	2349	2289	2371	2255	2288	2423	2056
Sr	1849	1545	1847	1805	1547	1649	1550	1655	1671	1806	1667
Zn	550	810	560	590	770	620	680	700	640	650	640
Zr	279	427	292	320	465	362	470	422	413	393	426
Ba	1201	1284	1194	1149	1368	1266	1328	1425	1313	1592	1467
V	940	842	938	846	822	826	808	893	898	998	919
Mo	557	487	518	574	465	539	421	437	462	521	522
Tl	197	168	134	165	167	190	192	185	180	156	159
As	279,1	250,9	312,9	120,7	239,9	185,5	226,3	211,7	125,3	230,5	204,4
La	297	332	260	277	264	263	239	236	259	308	298
Ce	1453	1706	1387	1430	1751	1558	1607	1765	1433	1873	1867
Pr	60	68	51	52	48	49	44	46	48	60	60
Nd	232	263	207	212	192	207	181	180	201	244	248
Sm	48	56	43	41	39	39	35	36	39	47	48
Eu	11	13	10	10	9	9	8	9	9	11	11
Gd	51	62	47	48	47	44	43	41	45	54	55
Tb	8	9	7	7	7	7	6	6	6	8	8
Dy	44	51	41	39	40	39	36	34	40	45	46
Ho	9	10	9	9	9	8	8	8	8	9	9
Er	25	27	24	25	25	23	23	22	25	26	25
Tm	4	4	4	4	4	3	3	3	3	4	4
Yb	23	25	21	21	24	22	21	20	22	22	23
Lu	3	4	3	4	4	3	3	3	4	3	3
Y	179	187	192	180	168	154	151	141	163	153	155
Sc	4	12	4	4	8	6	6	5	6	6	8
SUM	2451	2830	2310	2362	2640	2434	2413	2556	2311	2872	2868

(3) NODULE-LIKE										
Sample	ML-78b	ML-14b	DC-05a	DC-20b	DC-29a	ML-73a	ML-75b	ML-41e	ML-78a	ML-14a
SiO_2	4,14	2,82	2,70	3,34	2,65	2,75	3,37	1,86	3,08	1,50
Al_2O_3	2,25	1,79	1,30	1,18	1,15	1,00	1,63	0,99	1,20	1,07
Fe_2O_3	22,46	21,63	20,60	23,41	22,35	24,83	21,73	19,15	23,07	23,65
MnO	24,49	24,55	24,93	24,85	27,37	25,21	25,28	25,60	23,03	24,66
CaO	3,21	3,25	4,85	3,31	3,35	3,25	3,50	3,38	3,13	4,74
MgO	2,39	2,39	2,05	1,95	2,10	1,87	2,29	1,94	1,82	2,21
Na_2O	1,83	1,67	1,80	1,80	1,82	1,79	2,07	1,74	1,82	1,67
K_2O	0,52	0,43	0,49	0,45	0,44	0,40	0,47	0,38	0,35	0,36
TiO_2	1,16	1,65	1,60	1,73	1,71	1,69	1,73	1,43	1,27	1,64
P_2O_5	1,18	1,23	1,72	1,10	0,99	1,05	1,24	1,05	1,00	1,24
LOI	33,8	35,5	34,8	34,0	33,2	33,3	33,8	39,7	37,9	34,3
SUM	97,43	96,91	96,84	97,12	97,13	97,14	97,11	97,22	97,67	97,04
Co	7680	10020	11480	10000	11440	9810	11010	12500	8560	7070
Ni	4228	4775	4066	3996	4019	2968	3889	3623	2493	4198
Cu	824	694	501	514	422	270	522	337	260	276
Pb	1466	2370	2556	2546	2574	2918	2396	2647	1979	2674
Sr	1340	1650	1753	1687	1567	1801	1623	1511	1561	2034
Zn	870	800	650	660	630	640	710	640	610	550
Zr	401	427	375	436	382	392	413	299	369	397
Ba	1607	1432	1521	1430	1305	1433	1284	1072	1106	1507
V	876	840	864	849	837	940	839	745	878	1131
Mo	500	445	510	495	486	510	434	498	497	516
Tl	178	280	243	251	270	209	193	198	147	208
As	115,0	131,9	65,8	189,0	170,8	271,8	176,4	202,6	185,4	285,4
La	219	225	241	275	249	314	263	225	323	257
Ce	1271	1364	1609	1516	1278	1885	1441	1214	1315	1565
Pr	45	41	46	52	48	59	49	42	66	50
Nd	193	170	182	215	180	241	211	176	279	200
Sm	37	34	36	42	40	48	40	34	54	41
Eu	9	8	8	10	9	11	9	8	12	9
Gd	42	41	41	48	43	53	48	37	61	47
Tb	6	6	6	7	6	8	7	6	9	7
Dy	36	35	35	41	38	45	41	31	53	40
Ho	7	8	7	9	8	10	9	7	10	9
Er	21	23	20	26	23	28	26	20	29	26
Tm	3	3	3	4	3	4	4	3	4	4
Yb	18	21	19	23	21	24	23	18	25	24
Lu	3	3	3	4	3	4	4	3	4	4
Y	131	163	150	170	167	182	175	137	173	186
Sc	9	5	4	6	5	6	6	4	9	4
SUM	2050	2150	2411	2447	2120	2919	2354	1963	2427	2472

b) *Young non-phosphatized crusts*

Table 2: Chemical composition of ferromanganese crusts.

Mn and Fe are the main elements in young non-phosphatized crust, with an average concentration (wt %) of 19.04 and 16.07, respectively. The Fe/Mn ratios average 0.85 which indicates the hydrogenous origin of these deposits. In these crusts the average concentrations (wt %) of Co, Ni, Pb, Ti, Cu and Ce are 0.92, 0.34, 0.25, 0.03, 0.92 and 0.15, respectively. However, in old phosphatized crust, the main elements are CaO and P_2O_5, with an average of 34.77% and 15.93%, respectively. In this type of crust the ore forming elements content is lowest and only Ni is higher (0.41wt %), whereas the average concentrations (wt %) of Co, Ti, Cu, Pb and Ce are 0.18, 0.04, 0.2, 0.02 and 0.02, respectively. The geochemical signature of Fe–Mn crusts is interpreted using the Fe - Mn - (Ni+Co+Cu) x 10 diagram, with all our data points plotting in the field of hydrogenic crusts (Figure 8). The (Mn+Fe)/Ti ratios in samples of young non-phosphatized crust vary from 31.72 to 49.86 and in old phosphatized crust between 46.63 and 87.19. The average growth rate of non-phosphatized crust were calculated using empirical law [49], with values of 1.75 mm/Ma, 2.24 mm/Ma and 1.70 mm/Ma for plate-like concretion, plate-like flat and nodule-like crusts, respectively.

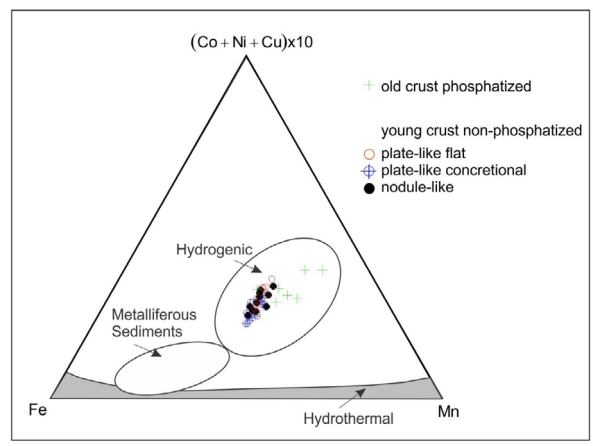

Figure 8: Ternary diagram after Bonatti, *et al*. [50], modified by Toth [51] for the classification of submarine ferromanganese deposits and adapted after Canet, *et al*. [52].

Regarding major oxides young non-phosphatized Fe-Mn-rich crusts are enriched in SiO_2, Na_2O, K_2O that concentrate in the clastic fractions (quartz and feldspar) as described from thin sections. The concentrations of trace elements in young non-phosphatized crusts are also higher than in old phosphatized crusts, except for phosphate. In comparison, the old phosphatized crusts are enriched in carbonate, phosphate and yttrium.

According Bau, et al. [53], "*The Ce_{SN}/Ce_{SN*} ratio is the simplest approach to quantify redox related decoupling of Ce from the other REY, which produces Ce anomalies in REY_{SN} patterns and the Y_{SN}/Ho_{SN} ratio reveals decoupling of the geochemical twins Y and Ho, which produces Y_{SN} anomalies in REY_{SN} patterns. The bivariate diagram of Ce_{SN}/Ce_{SN*} ratio vs Y_{SN}/Ho_{SN} ratio show different groups of ferromanganese deposits, i.e., hydrogenous, diagenetic and hydrothermal*". On the Rio Grande Rise crusts, young non phosphatized plot in hydrogenous and old phosphatized plot in diagenetic type (Figure 9). This diagram show that old phosphatized crusts is diagenetic origin.

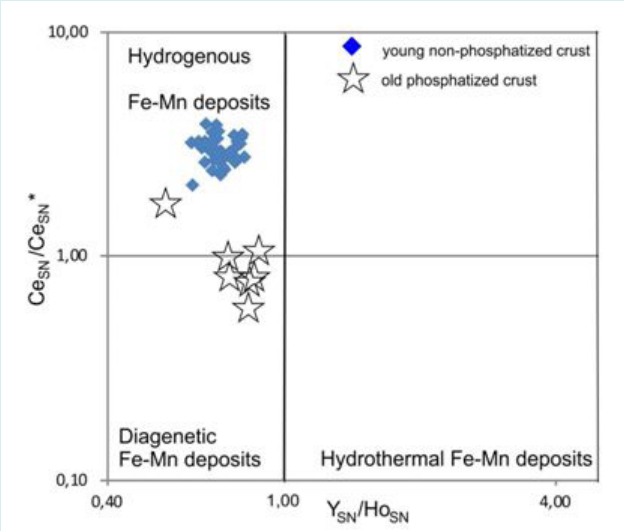

Figure 9: Marine Fe–Mn oxide deposits in graphs of Ce_{SN}/Ce_{SN*} ratio vs Y_{SN}/Ho_{SN} ratio for the Rio Grande Rise crusts (Compiled and adapted from Bau, et al.) [53].

The content of REE varies greatly between the young non-phosphatized and the old phosphatized crusts. In young non-phosphatized crusts the total REE contents vary from 2041 to 2866 ppm, with an average of 2420 ppm. The average abundances of light-REE and heavy-REE are, respectively, 2100 ppm and 264 ppm. The LREE/HREE ratios vary from 5.23 to 8.13, with an average of 6.68. Among all REE elements Ce is the most abundant, with an average content of 1514 ppm. In old phosphatized crusts the total REE contents vary from 424 to 1341 ppm, with an average of 919 ppm. The average abundances of light-REE and heavy-REE are, respectively, 590 ppm and 328 ppm. The LREE/HREE ratios vary from 1.24 to 3.48, with an average of 1.8. The PAAS-normalized REE patterns of ferromanganese crusts from the Rio Grande Rise differ significantly between the young non-phosphatized and old phosphatized types, e.g., flat pattern of the other REE elements, with high positive Ce anomaly and enriched approximately ten times the PAAS (Figure 10). However the phosphatized crusts do not have Ce anomalies and have fewer REE elements.

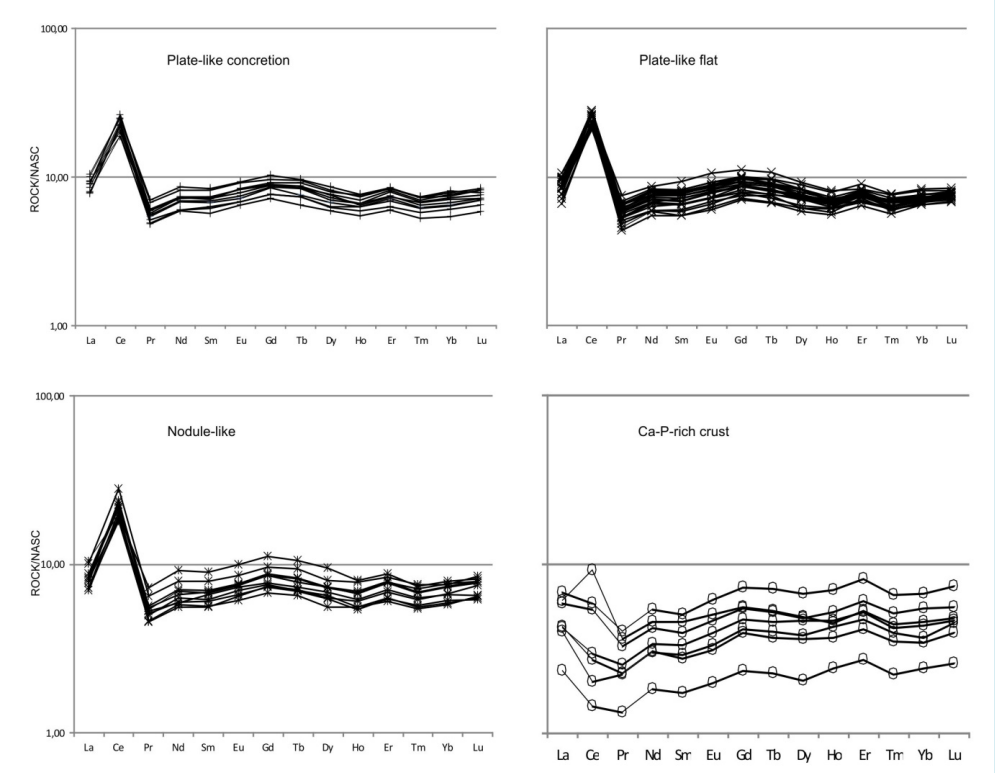

Figure 10: PAAS-normalized REE pattern of ferromanganese crusts from the Rio Grande Rise. a) young non phosphatized crusts; b) old phosphatized crusts.

Also according Bau, et al. [53], "*The REY distribution in hydrogenetic Fe–Mn crusts represents an exchange equilibrium suggests that (i) at a given Fe/Mn ratio, the absolute REY concentration in a hydrogenetic Fe–Mn crust is largely controlled by the dissolved REY concentration in ambient seawater; and (ii) hydrogenetic Fe–Mn crusts are characterized by very similar REY distribution patterns regardless of their place of origin as long as there was no significant difference between dissolved REY concentrations and distributions in their depositional environments during growth*." In Rio Grande Rise crusts, young non phosphatized show positive anomaly of Ce and negative anomaly of Y and old phosphatized show positive Y anomaly, which distinguish the two crusts types (Figure 10).

Microbial Diversity

On the Fe-Mn crusts samples of Rio Grande Rise, the prevalent classes identified were Gammaproteobactéria (57-24%), Alphaproteobactéria (17-16%) and Nitrosospharia (17-7%), and in the Fe-Mn encrusted coral skeletons, the prevalent class was related to Gammaproteobacteria (27%), Alphaproteobacteria (20%), Planctomycetacia (7%), Nitrososphaeria (5%), and Deltaproteobacteria (5%), according to the studies carried out by Bergo *et al.* (2021).

$^{87}Sr/^{86}Sr$ indirect dating

$^{87}Sr/^{86}Sr$ analyses on phosphatized ferromanganese crusts samples yielded ratios of 0.70833 ± 2 and 0.70880 ± 2. Comparing the $^{87}Sr/^{86}Sr$ ratio of the samples to the curve of the Sr isotope composition of the oceans through the Cenozoic, we suggest that analyzed materials crystallized between 21.7 and 14.5 Ma ago (Figure. 11 and 12, Table 3). These Sr isotope ratios represent isotope ratios without an age correction to subtract radiogenic ^{87}Sr produced by internal decay of ^{87}Rb after the time of deposition. Phosphate minerals and calcite have a low $^{87}Rb/^{86}Sr$ ratio (<0.01) with a high concentration of unradiogenic Sr [54,55]. The age correction is almost negligible for the Sr isotope. However, data must be interpreted with care because Sr ages of carbonate and carbonate fluorapatite are susceptible to diagenetic effects: incorporation of Sr during the crystallization of authigenic minerals [48].

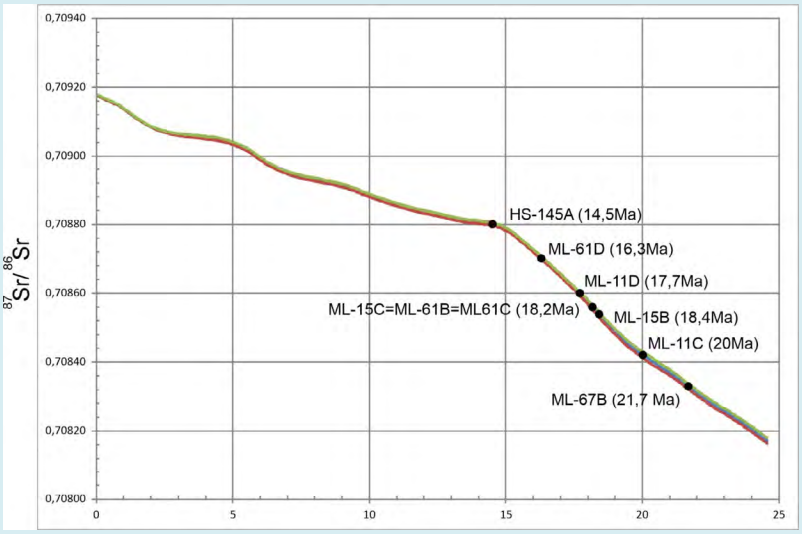

Figure 11: Diagram for the period 0-25 Ma (using Lowess Fit, Version 5, provided by author McArthur of London's Global University), with the main ages of de ferromanganese crusts of Rio Grande Rise.

Figure 12: Ferromanganese crusts samples used in the strontium isotopic analyses, with the age based on the curves of Lowess Fit (Figure 11).

No	Sample	Type	Age	Deep (i)	Deep (f)
1	DC-15	Ca-P rich Ferromanganese Crust		1022m	1013m
2		Ca-P rich Ferromanganese Crust	18.4 Ma		
3		Ca-P rich Ferromanganese Crust	18.2 Ma		
4	DC-61	Ca-P rich Ferromanganese Crust		1245m	1165m
5		Ca-P rich Ferromanganese Crust	16.4 Ma		
6		Carbonate vein			
7		Ca-P rich Ferromanganese Crust	16.2 Ma		
8	ML-11	Ca-P rich Ferromanganese Crust		1150m	1122m
9		Ca-P rich Ferromanganese Crust	20.0 Ma		
10		Ca-P rich Ferromanganese Crust			
11		Carbonate vein	17.7 Ma		
12	ML-67	Carbonate vein		1000m	950m
13		Ca-P rich Ferromanganese Crust	21.7 Ma		
14		Ca-P rich Ferromanganese Crust			
15		Ca-P rich Ferromanganese Crust			
16	HS-145	Limestone	14.5 Ma	850m	688m

Table 3: Ages of ferromanganese crusts based on strontium analyses, using Lowess Fit (Version 5), provided by author McArthur of London's Global University.

Discussion

On the Rio Grande Rise were identified an old phosphatized ferromanganese crust overlaid by a young non-phosphatized ferromanganese crust. The young non-phosphatized crust is enriched in cobalt whereas the phosphatized crust is depleted in this element. As phosphogenesis and Mn-oxide precipitation are distinct processes, the sequence of phosphates and Mn-Fe oxide layers can represents important indicators of changing paleoceanographic and paleoclimatic conditions [56]. According to these authors, the age of ferromanganese crust phosphatization in the North Atlantic might be significantly older than previously thought, up to 30 Ma old (in Tropic Seamount) and in the Pacific crust up to 40 Ma. The phosphatization event identified in the Rio Grande Rise was between 21.7 e 14.5 Ma. The large quantity of phosphorous may have derived from intensive chemical weathering on the continents or may be related to episodes of increased productivity and biogenic particle flux [56].

The main structures of the ferromanganese crusts are wave-layered, columnar, botryoidal and nodular, which are very common in stromatolites. Others observed structures are discontinuities such as erosional surface and/or depositional hiatus, both representing possible global change in the ocean. The concretion structures which are common in nodule-like and plate-like crusts have a phosphate core. This phosphate-rich core may represent the substrate which was incorporated during the deposition of the ferromanganese crusts.

Previous studies have shown that biomineralization may have played an important role in the formation of ferromanganese crust [11,12,14-16,19,57]. For example, the Mn oxides produced by Mn (II)-oxidizing bacteria can adsorb trace elements such as Co, Cu and Ni, leading to their concentration in the forming crusts [58]. Under anaerobic conditions, Mn (III) and Mn (IV) can be rapidly reduced by a variety of indirect and direct mechanisms, such as excretion of organic or inorganic reductants, or by bacterial respiration [59].

The geologic record of stromatolites clearly shows the extensive role that microbes have played in the evolution of the Earth´s environment [60]. The morphology and structures of stromatolites are the direct result of microbial activities and provide key insight into the nature of these ecosystems [61]. Microbial mats are multilayered communities that drive the biogeochemical cycling of key elements within the stromatolite ecosystem [62]. According to these authors, today with the advent of molecular high-through-put sequencing, ecotypes within mat community can be delineated and compared among different stromatolite communities, for example, hypersaline stromatolites of Shark Bay (Australia), the open ocean stromatolites of Highborne Cay (Bahamas), the flashwater stromatolites of

Ruidera Pool (Spain) and ferromanganese stromatolites of El Soplao Cave (N Spain). The study carried out by Foster & Green [62], based on analyses of 16S rRNA gene sequences, showed that the Shark Bay stromatolites appear to be dominated by *Alphaproteobacteria* (20%), *Actinobacteria* (16%) and *Cyanobacteria* (15%); and in the Highborne Cay the stromatolitic mats are dominated by *Alphaproteobacteria* (38%) and *Cyanobacteria* (18%).

The first reference to microbial diversity from ferromanganese crusts in deep-sea environment was published by Liao, et al. [16]. This study showed the great diversity of microbial mat that exists in the ferromanganese crusts occurring on the seamounts of the Western Pacific Ocean, next to the Philippine Sea. The results indicate that *Gammaproteobacteria* (23%) was the most dominant group, followed by *Alphaproteobacteria* (18%) and *Deltaproteobacteria* (17.5%), the non-proteobacteria groups accounting for 41% by mainly included *Acidobacteria* (7.7%), *Planctomycetes* (7.2%) and *Chloroflexi* (6.2%).

Nitahara, et al. [17] studying the Fe-Mn crusts of the old seamounts of the northwestern Pacific suggested that crust microbial communities play a role in biogeochemical cycling of C, N, S, Fe, and Mn, and imply that they contribute to the growth of Fe-Mn crusts. Were identified four metagenome-assembled genomes affiliated with *Thaumarchaeota*, *Alphaproteobacteria*, and *Gammaproteobacteria*.

Bergo, *et al.* [63] identified on the Fe-Mn crusts of Rio Grande Rise Bacterial and Archaeal composition varied in abundance or occurrence among samples. The authors described the microbial groups Proteobacteria (classes Gammaproteobacteria and Alphaproteobacteria), Thaumarchaeota (Nitrosopumilales), and Planctomycetes (classes Phycisphaerae) were abundant in all substrates. In Fe-Mn crust biofilm, the prevalent class was Nitrososphaeria (60-51%, Nitrosopumilales), Dehalococcoidia (20–7%, order SAR202 clade), Gammaproteobacteria (10–5%, orders Steroidobacterales and uncultivated UBA10353 marine group), Alphaproteobacteria (10–3%, orders Rhodovibrionales and SAR11), and Deltaproteobacteria (6–1%, orders SAR324 clade and NB1-j). The prevalent classes in the crusts were Gammaproteobacteria (57–24%, order Steroidobacterales, MBMPE27, and SAR86), Alphaproteobacteria (17–16%, order Rhodovibrionales), and Nitrososphaeria (17–7%, order Nitrosopumilales) and NC10 (9%, order Methylomirabilales).

Microbial assemblages in samples from the RGR showed the dominance of the classes Gammaproteobacteria, Alphaproteobacteria, and Deltaproteobacteria, as described for others Fe-Mn crusts deposits [57,64-66]. Biofilms with filamentous microorganisms associated with micro-stromatolitic growth bands have been described in the Fe-Mn nodules and crust surfaces [57,67-69].

From a geochemical perspective, the Ce anomaly was used as an environmental indicator of the ferromanganese crusts origin. Hydrogenous crusts, here considered hydrogenous/biogenic crusts (based on the evidence presented in this research) display positive anomaly whereas hydrothermal crusts show negative anomaly. The main characteristic of the Rio Grande Rise non phosphatised crusts is a highly positive Ce anomaly. The Fe/Mn ratio is another parameter used for differentiate the ferromanganese crusts. These crusts generally have Fe/Mn ratios between 0.4 and 1.2 lower than the ratios in hydrogenous crusts of the continental margin which range between 1 and 3, mostly 1.3 to 1.8 [9]. On the Rio Grande Rise the crusts have Fe/Mn ratios averaging 0.85 which indicates a hydrogenous/biogenic origin [70-75].

Conclusion

The ferromanganese crusts of the Rio Grande rise are of two main types (non-phosphatized and phosphatized) and occur in the form of plates fixed on the bedrock (volcanic and limestone rocks), also in the form of nodules containing rock core and detached from the surface. The main mineralogy composition is Fe-vernadite, but also has carbonate-fluorapatite and calcite that are present in all phosphatized samples [76-80].

The wavy-layered, columnar and botryoidal structures identified in the ferromanganese crusts are very common in stromatolites. The microbial assemblages in samples from the Rio Grande Rise are similar to those found in stromatolites and also in ferromanganese crusts from other regions of the planet. Based on the evidence presented in this research, the ferromanganese crusts are not only similar to stromatolites, but may also be a kind of black stromatolites that inhabited the seabed [81-84].

Funding

This research is part of the “Programme for Prospecting and Exploitation of Mineral Resources in the International South Atlantic and Equatorial Area (PROAREA)”, of the project “Prospecting and Exploration of Ferromanganese Crusts of the Rio Grande Rise” and was supported by Geological Survey of Brazil, Ministry of Mines and Energy, Federal Government of Brazil.

Declaration

Conflict of Interest: The authors declare no competing interests.

References

1. Hein JR, Mizell K, Koschinsky A, Conrad TA (2013) Deep-ocean mineral deposits as a source of critical metals for high- and green-technology applications: Comparison with land-based resources. Ore Geology Reviews 51: 1-14.

2. Wang XH, Gan L, Müller WEG (2009a) Contribution of biomineralization during growth of polymetallic nodules and ferromanganese crusts from the Pacific Ocean. Front Mater Sci China 3(2): 109-123.

3. González FG, Somoza L, Maldonado R, Lunar R, Martínez Frías J, et al. (2010) High Technology Elements in Co-Rich ferromanganese crusts from the Scotia Sea. Revista de la Sociedad Española de Mineralogia 13: 113-114.

4. Korotkina OA, Kogarko LN, Bazilevskaya ES, Kurbakova V (2010) Geochemistry of Fe–Mn Deposits of the Atlantic Ocean (Strakhov Basin, Elena Seamount, and Cape Verde Quadrangle). Geochemistry International 48: 1166-1176.

5. Pulyaeva IA, Hein JR (2010) Paleoceanographic conditions during the formation of Fe-Mn crusts from the Pacific Ocean: biostratigraphic and compositional evidence. Toward the Sustainable Development of Marine Minerals: Geological, Technological, and Economic Aspects. UMI 2010 - Gelendzhik, Russia.

6. Hein JR, Conrad TA (2012) Cooper-nickel-rich, amalgamated ferromanganese crust-nodule deposits from Shatsky Rise, NW Pacific. Geochemistry Geophysics Geosystems 13(10): 1-13.

7. Zhenguo Z, Yuansheng D, Lianfeng G, Ying Z, Guoyuan S, et al. (2012) Enrichment of REEs in polymetallic nodules and crusts and its potential for exploitation. Journal of Rare Earths 30(6): 621-626.

8. Hein JR, Koschinsky A (2014) Deep-Ocean Ferromanganese Crusts and Nodules. In: Holland H, Turekian K (Chief Eds.), Treatise on Geochemistry, In: Scott SD (Ed), Geochemistry of Mineral Deposits 13, Elsevier, Amsterdan, Netherlands, Second Edition, pp: 273-291.

9. Hein JR, Koschinsky A, Bau M, Manheim FT, Kang J, et al. (2000) Cobalt-rich Ferromanganese Crusts in Pacific. In: Cronan DS (Ed.), Handbook of Marine Mineral Deposits, CRC Press, London, UK, pp: 239-279.

10. Hein JR, Koschinsky A, Halliday AN (2003) Global occurrence of tellurium-rich ferromanganese crusts and a model for the enrichment of tellurium. Geochimica et Cosmochimica Acta 67(6): 1117-1127.

11. Wang X, Muller WEG (2009b) Marine biominerals: perspectives and challenges for polymetallic nodules and crusts. Trends Biotechnol 27(6): 375-383.

12. Wang XH, Schloßmacher U, Natalio F, Schröder HC, Wolf SE, et al. (2009c) Evidence for biogenic processes during formation of ferromanganese crusts from the Pacific Ocean: implications of biologically induced mineralization. Micron 40(5-6): 526-535.

13. Liao L, Xu XW, Jiang XW, Wang CS, Zhang DS, et al. (2011) Microbial diversity in deep-sea sediment from the cobalt-rich crust deposit region in the Pacific ocean. FEMS Microbiology Ecology 78(3): 565-585.

14. Wang Y, Peine F, Schmidt A, schröder HC, Wiens M, et al. (2011) Concept of biogenic ferromanganese crust formation: coccoliths as bioseeds in crusts from Central Atlantic Ocean (Senghor Seamount/Cape verde). Natural Product Communications 6(5): 1-10.

15. Avdonin VV, Eremin NI, Mel´nikov ME, Sergeva NE (2013a) Meso-Cenozoic ferromanganese ore genesis in the world ocean. Doklady Earth Science 451: 824-826.

16. Avdonin VV, Mel´nikov ME, Sergeeva NE (2013b) The submicroscopic structures of Mesozoic-Cenozoic Fe-Mn stromatolites. Moscow University Geology Bulletin 68: 289-294.

17. Nitahara S, Kato S, Usui A, Urabe T, Suzuki K, et al. (2017) Archaeal and bacterial communities in deep-sea hydrogenetic ferromanganese crusts on old seamounts of the northwestern Pacific. PLoS ONE 12(2): e0173071.

18. Kato S, Hirai M, Ohkuma M, Suzuki K (2019) Microbial metabolisms in an abyssal ferromanganese crust from the Takuyo-Daigo Seamount as revealed by metagenomics. PLoS ONE 14(11): e0224888.

19. Wang X, Gan L, Wiens M, Schloßmacher, Schröder HC, et al. (2012) Distribution of microfossils within polymetallic nodules: biogenic clusters within manganese layers. Marine Biotechnology 14(1): 96-105.

20. Bogdanova OU, Gorshkov I, Novikov GV, Bogdanov YA (2008) Mineralogy of morphogenetic types of ferromanganese deposits in the world ocean. Geology of Ore Deposits 50: 462-469.

21. Jeong KS, Jung HS, Kang JK, Morgan CL, Hein JR (2000) Formation of ferromanganese crusts on northwest intertropical Pacific seamounts: electron photomicrography and microprobe chemistry. Marine Geology 162: 541-559.

22. Kim J, Hyeong K, Yoo CM, Moon JW, Kim KH, et al. (2005) Textural and geochemical characteristics of Fe-Mn crusts from four seamounts near the Marshall Islands, western Pacific. Geosciences Journal 9: 331-338.

23. Hein JR, Yeh HW, Gunn SH, Sliter WV, Benninger LM, et al. (1993) Two major Cenozoic episodes of phosphogenesis recorded in Equatorial Pacific seamount deposits. Paleoceanography 8(2): 293-319.

24. Halbach P, Sattler C, Teichmann F, Wahsner M (1989) Cobalt-rich and platinum bearing manganese crust deposits on seamounts: Nature, formation, and metal potential. Marine Mining 8: 23-39.

25. Nayak B, Kumar Das S, Munda P (2013) Biogenic signature and ultra-microfossils in ferromanganese nodules of the Central Indian Ocean Basin. Journal of Asian Earth Sciences 73: 296-305.

26. Jenkyns HC (1977) Fossil Nodules. In: Grasby GP (Ed.), Marine Manganese Deposits, Elsevier Oceanography Series 15: 87-108.

27. Akai J, Iida A, Akai K (1997) Mn and Fe minerals of possible biogenic origin from two Precambrian stromatolites in Western Australia. Journal of Geological Society of Japan 103(5): 484-488.

28. Seckback J (2011) Introduction to stromatolites. In: Tewari V, Seckback J (Eds.), Stromatolites: interaction of microbes with sediments. Cellular Origin, Life in Extreme Habitats and Astrobiology, New York, NYIn: Tewari & Seckback 18: IX.

29. Awramik SM, Grey K (2005) Stromatolites: Biogenicity, Biosignatures, and Bioconfusion. In: Hoover RB, Levin GY, Rozanov AY, Gladstone GR (Eds.), Astrobiology and Planetary Missions. Proc Of SPIE 5960: 1-9.

30. Föllmi KB, Delamette M, Ouwehand PJ (2011) Aptian to Cenomanian Deeper-Water Hiatal Stromatolites from the Northern Tethyan Margin. In: Tewari V, Seckback J (Eds.), Stromatolites: interaction of microbes with sediments. Cellular Origin, Life in Extreme Habitats and Astrobiology, Springer, New York, pp: 161-186.

31. Lozano RP, Rossi C (2012) Exceptional preservation of Mn-oxidizing microbes in cave stromatolites (El Soplao, Spain). Sedimentary Geology 255-256: 42-55.

32. Farias ME, Poiré DG, Arrouy MJ, Albsrracin VH (2011) Modern stromatolite ecosystems at alkaline and hypersaline hight-altitude lakes in the Argentinean Puna. In: Tewari V, Seckback J (Eds.), Stromatolites: interaction of microbes with sediments. Cellular Origin, Life in Extreme Habitats and Astrobiology. Springer, New York, pp: 431-441.

33. Duncan RA (1981) Hot-spots in the southern oceans - An absolute frame of reference for the motion of the Gondwana continents, Tectonophysics 74(1-2): 29-42.

34. Morgan WJ (1981) Hotspot tracks and the opening of the Atlantic and Indian oceans. In: Emiliani C (Ed.), The Sea: The Oceanic Lithosphere, Wiley-Interscience, New York 7: 443-487.

35. O'Connor JM, Duncan RA (1990) Evolution of the Walvis Ridge-Rio Grande Rise hot spot system: implications for African and South American plate motions over plumes, Journal of Geophysical Research 95(B11): 17475-17502.

36. Gamboa LAP, Rabinowitz PD (1984) The evolution of the Rio Grande Rise in the Southwest Atlantic Ocean, Marine Geology 58(1-2): 35-58.

37. Rohde JK, Bogaard Pvd, Hoernle K, Hauff F, Werner R (2013) Evidence for an age progression along the Tristan-Gough volcanic track from new $^{40}Ar/^{39}Ar$ ages on phenocryst phases, Tectonophysics 604: 60-71.

38. Mohriak WU, Nóbrega M, Odegard ME, Gomes BS, Dickson WG (2010) Geological and geophysical interpretation of the Rio Grande Rise SE Brazilian margin: extensional tectonics and rifting of continental and oceanic crusts. Petroleum Geosciences 16(3): 231-245.

39. Ulbrich HHGJ, Gomes CB (1981) Alkaline rocks from continental Brazil. Earth-Science Reviews 17(1-2): 135-154.

40. Fodor RV, Husler JW, Kumar N (1977) Petrology of volcanic rocks from an aseismic ridge: implications for the origin of the Rio Grande Rise, South Atlantic Ocean, Earth and Planetary Science Letters 35(2): 225-233.

41. Ussami N, Chaves C, Chaves CAM, Marques LS, Ernesto M (2012) Origin of the Rio Grande Rise-Walvis Ridge reviewed integrating palaeogeographic reconstruction, isotope geochemistry and flexural modelling. In: Mohriak WU, Danforth A, Post PJ, et al. (Eds.), Conjugate Divergent Margins, Geological Society, London, Special Publications 369: 129-146.

42. Santos RV, Ganade CE, Lacasse CM, Costa ISL, Pessanha I, et al. (2019) Dating Gondwanan continental crust at the Rio Grande Rise, South Atlantic. Terra Nova 31(5): 424-429.

43. Operto S, Charvis P (1995) Kerguelen Plateau: a volcanic passive margin fragment?. Geology 23(2): 137-140.

44. Gladczenko TP, Coffin MF (2001) Kerguelen Plateau crustal structure and basin formation from seismic and gravity data, Journal of Geophysical Research 106(B8): 16583-16601.

45. Frey FA, Coffin MF, Wallace PJ, Weis D (2003) Leg 183 synthesis: Kerguelen Plateau-Broken Ridge - a large igneous province. In: Frey FA, Coffin MF, Wallace PJ, et al. (Eds.), Proceedings of the Ocean Drilling Program, Scientific Results 183: 1-48.

46. Regelous M, Gamble J, Turner S (2010) Mechanism and timing of Pb transport from subducted oceanic crust and sediment to the mantle source of arc lavas. Chemical Geology 273(1-2): 46-54.

47. Barker PF, Buffler RT, Gamboa LA (1981) A seismic reflection study of the Rio Grande Rise. In: Barker PF, Carlson RL, Johnson DA (Eds.), Initial Reports of the Deep Sea Drilling Project 72: 499-517.

48. Souza KG, Fontana RL, Mascle J, Macedo JM, Mohriak WU, et al. (1993) The southern Brazilian margin: an example of a South Atlantic volcanic margin. Third International Congress of the Brazilian Geophysical Society, Rio de Janeiro, pp: 1336-1341.

49. Puteanus D, Halbach P (1988) Correlation of Co concentration and growth rate – A method for age determination of ferromanganese crusts. Chemical Geology 69(1-2): 73-85.

50. Bonatti E, Kraemer T, Rydell H (1972) Classification and genesis of submarine iron-manganese deposits. In: Horn RD (Ed.), Ferromanganese deposits of the ocean floor. Aren House, Harriman, pp. 473-489.

51. Toth JR (1980) Deposition of submarine crusts rich in manganese and iron. Geol Soc Amer Bull 91(1): 44-54.

52. Canet C, Prol-Ledesma RM, Bandy WL, Schaaf P, Linares C, et al. (2008) Mineralogical and geochemical constraints on the origin of ferromanganese crusts from Rivera Plate (western margin of Mexico). Marine Geology 251(1-2): 47-59.

53. Bau M, Schmidt K, Koschinsky A, Hein JR, Kuhn T, et al. (2014) Discriminanting different genetic types of marine ferromanganese crusts and nodules based on rare earth elements and yttrium. Chemical Geology 381: 1-9.

54. Faure G, Powell JL (1972) Strontium Isotope Geology. Springer-Verlag, Berlin, New York, pp: 188.

55. Faure G (2001) Origin of Igneous Rocks - the Isotopic Evidence. Springer-Verlag, Heidelberg, pp: 496.

56. Koschinsky A, Halbach P, Hein JR, Mangini A (1996) Ferromanganese crusts as indicator for paleoceanographic events in the NE Atlantic. Geol Rundsch 85: 567-576.

57. Wang X, Schlossmacher U, Wiens M, Schroeder HC, Muller WEG (2009) Biogenic origin of polymetallic nodules from the Clarion-Clipperton Zone in the Eastern Pacific Ocean: electron microscopic and EDX evidence. Mar Biotechnol 11(1): 99-108.

58. Nealson KH (2006) The manganese-oxidizing bacteria. In: Dworkin M, Falkow S, Rosenberg E, et al. (Eds.), The Prokaryotes, Springer, New Dalhi, India, pp: 222-231.

59. Nealson KH, Rosson RA, Myers CR (1989) Mechanisms of oxidation and reduction of manganese. In: Beveridge TJ, Doyle R (Eds.), : Metal ions and bacteria, pp: 383-411.

60. Kasting JF (2001) Earth History. The rise of atmospheric oxygen. Science 293(5531): 819-820.

61. Burne RV, Moore LS (1987) Microbialites: organosedimentary deposits of benthic microbial communities. Palaios 2(3): 241-254.

62. Foster JS, Green SJ (2011) Microbial Diversity in Modern Stromatolites. In: Tewari V, Seckback J (Eds.), Stromatolites: interation of microbes with sediments. Cellular Origin, Life in Extreme Habitats and Astrobiology, New York, pp: 383-405.

63. Bergo NM, Bendia AG, Ferreira JCN, Murton BJ, Brandini FP, et al. (2021) Microbial Diversity of Deep-Sea Ferromanganese Crust Field in the Rio Grande Rise, Southwestern Atlantic Ocean. Microbial Ecology 82: 344-355.

64. Lindh MV, Maillot BM, Shulse CN, Gooday AJ, Amon DJ, et al. (2017) From the surface to the deep-sea: bacterial distributions across polymetallic nodule fields in the Clarion-Clipperton zone of the Pacific Ocean. Front Microbiol 8: 1-12.

65. Shulse C, Maillot B, Smith CR, Church MJ (2016) Polymetallic nodules, sediments, and deep waters in the equatorial North Pacific exhibit highly diverse and distinct bacterial, archaeal, and microeukaryotic communities. Microbiol Open 6(2): e00428.

66. Wu YH, Liao L, Wang CS, Ma WL, Meng FX, et al. (2013) A comparison of microbial communities in deep-sea polymetallic nodules and the surrounding sediments in the Pacific Ocean. Deep-Sea Res I Oceanogr Res Pap 79: 40-49.

67. Burnett BR, Nealson KH (1981) Organic films and

microorganisms associated with manganese nodules. Deep-Sea Res I Oceanogr Res Pap 28(6): 637-645.

68. Jiang XD, Sun XM, Guan Y (2017) Biogenicmineralization in the ferromanganese nodules and crusts from the South China Sea. J Asia Earth Sci 171: 46-59.

69. Templeton AS, Knowles EJ, Eldridge DL, Arey BW, Dohnalkova AC, et al. (2009) A seafloor microbial biome hosted within incipient ferromanganese crusts. Nat Geosci 2(12): 872-876.

70. Alvey B, Kusznir NJ, Roberts AM (2011) Detached micro-continents off shore southern Brazil: crustal thickness from gravity inversion and plate reconstruction. AAPG Annual Conference and Exhibition.

71. Arrhenius G (1963) Pelagic Sediments. In: Hill MN (Ed.), The Sea, Wiley-Interscience, New York 3: 655-727.

72. Camboa LAP, Rabinowitz PD (1984) The Evolution of the Rio Grande Rise in the South Atlantic Ocean. Marine Geology 58(1-2): 35-58.

73. Cameron EN (1961) Ore Microscopy. Willey, New York, pp: 249.

74. Ernesto M, Marques LS, Piccirillo EM, Molina EC, Ussami N, et al. (2002) Paraná Magmatic Province - Tristan da Cunha plume system: fixed v. mobile plume, petrogenetic considerations and alternative heat sources. Journal of Volcanology and Geothermal Research 118(1-2): 15-36.

75. Gibson SA, Thompson RA, Dickin AP, Leonardos OH (1995) High-Ti and low-Ti mafic potassic magmas: key to plume-lithosphere interactions and continental flood basalts genesis. Earth and Planetary Science Letters 136(3-4): 149-165.

76. Marques LS, Dupre B, Piccirillo EM (1999) Mantle source compositions of the Paraná Magmatic Province (southern Brazil): evidence from trace element and Sr-Nd-Pb isotope geochemistry. Journal of Geodynamics 28(4-5): 439-458.

77. McDowell S, Kumar N, Jacobi RD, Johnson DA, Bunce ET (1977) Regional setting of site 357, north flank of Rio Grande Rise. In: Barker PF, Carlson RL, Johnson DA, et al. (Eds.). Initial Reports of the Deep Sea Drilling Project 42: 955-969.

78. Peate D, Hawkesworth CJ, Mantovani MSM, Rogers NW, Turner SP (1999) Petrogenesis and stratigraphy of the high-Ti/Y Urubici magma type in the Paraná flood basalt province and implications for the nature of 'Dupal'-type mantle in the South Atlantic Region. Journal of Petrology 40(3): 451-473.

79. Piccirillo EM, Civetta L, Petrini R, Longinelli A, Bellieni G, et al. (1989) Regional variations within the Paraná flood basalts (Southern Brazil): evidence for sub-continental mantle heterogeneity and crustal contamination. Chemical Geology 75(1-2): 103-122.

80. Sousa IMC, Santos RV, Koschinsky A, Bau M, Wegorzewski AV, et al. (2021) Mineralogy and chemical composition of ferromanganese crusts from the Cruzeiro do Sul Lineament - Rio Grande Rise, South Atlantic. Journal of South American Earth Sciences 108: 103207.

81. Szatmari P, Mohriak WU (1995) Plate model of post-breakup tectonomagmatic activity in SE Brazil and the adjacent Atlantic. V Simpósio Nacional de Estudos Tectônicos – SNET, Gramado, RS, pp: 213-214.

82. Thompson G, Humphris S, Shilling JG (1983) Petrology and geochemistry of basaltic rocks from the Rio Grande Rise, South Atlantic, Deep Sea Drilling Project Leg 72, Hole 516F. In: Barker PF, Carlson RL, et al. (Eds.), Initial Reports of the Deep Sea Drilling Project.

83. Wang XH, Zhou LP, Wang YM, Zhang XH, Liu XM, et al. (2008) Paleoenvironmental implications of high-density records in Co-rich seamount crusts from the Pacific Ocean. Science in China Series D: Earth Sciences 51: 1460-1469.

84. Weaver BL, Marsh NG, Tarney J (1983) Trace element geochemistry of basaltic rocks recovered at Site 516F, Rio Grande Rise, DSDP Leg 72. In: Barker PF, Carlson RL, et al. (Eds.), Initial Reports of the Deep Sea Drilling Project, 72: 451-456.